

| REPORT DOCUMENTATION PAGE | | | <i>Form Approved</i> OMB No. 0704-0188 | |
|---|------------------------------------|---------------------------------------|--|---|
| Public reporting burden for this collection of information is estimated to average 1 hour per response, including the time for reviewing instructions, searching existing data sources, gathering and maintaining the data needed, and completing and reviewing this collection of information. Send comments regarding this burden estimate or any other aspect of this collection of information, including suggestions for reducing this burden to Department of Defense, Washington Headquarters Services, Directorate for Information Operations and Reports (0704-0188), 1215 Jefferson Davis Highway, Suite 1204, Arlington, VA 22202-4302. Respondents should be aware that notwithstanding any other provision of law, no person shall be subject to any penalty for failing to comply with a collection of information if it does not display a currently valid OMB control number. PLEASE DO NOT RETURN YOUR FORM TO THE ABOVE ADDRESS. | | | | |
| 1. REPORT DATE (DD-MM-YYYY) 07/06/2012 | | 2. REPORT TYPE Final Report | | 3. DATES COVERED (From - To) 4/1/05 - 3/31/11 |
| 4. TITLE AND SUBTITLE Development Of Toughened and Multifunctional Nanocomposites for Ship Structures | | | 5a. CONTRACT NUMBER | |
| | | | 5b. GRANT NUMBER N00014-1-0552 | |
| | | | 5c. PROGRAM ELEMENT NUMBER | |
| 6. AUTHOR(S) C. T. Sun | | | 5d. PROJECT NUMBER | |
| | | | 5e. TASK NUMBER | |
| | | | 5f. WORK UNIT NUMBER | |
| 7. PERFORMING ORGANIZATION NAME(S) AND ADDRESS(ES) Purdue University West Lafayette, Indiana 47907 | | | 8. PERFORMING ORGANIZATION REPORT NUMBER | |
| 9. SPONSORING / MONITORING AGENCY NAME(S) AND ADDRESS(ES) Office of Naval Research One Liberty Center 875 North Randolph Street Arlington, VA 22203-1995 | | | 10. SPONSOR/MONITOR'S ACRONYM(S) | |
| | | | 11. SPONSOR/MONITOR'S REPORT NUMBER(S) | |
| 12. DISTRIBUTION / AVAILABILITY STATEMENT DISTRIBUTION UNLIMITED | | | | |
| 13. SUPPLEMENTARY NOTES | | | | |
| 14. ABSTRACT This report consists of two parts. The objective of the first part of the research was to use a sol-gel in-situ produced silica nanoparticle-modified epoxy to manufacture fiber composites in order to enhance the mechanical properties of fiber composites. Vacuum assisted resin transfer molding (VARTM) process was used to fabricate unidirectional E-glass fiber reinforced silica/epoxy nanocomposites. Off-axis composite specimens with and without silica nanoparticles were tested to compare the compressive strength. A method for extracting the longitudinal compressive strength of the GFRP was developed based on the off-axis test data. Moreover, a microbuckling model was employed to predict the compressive strength based on the stress-strain curve of the silica nanocomposite. In the second part of the research, resonators are inserted into the core to provide a new degree of freedom in motion. Models for this new sandwich structure were first constructed. These models were subsequently employed to study wave propagation and the bandgap structure in the sandwich structure. Finally, sandwich specimens were manufactured and dynamic experiments were conducted to verify the analytical results | | | | |
| 15. SUBJECT TERMS Fiber composite, nanoparticle, nanocomposite, compressive strength, off-axis test, sandwich structures, dynamic response, wave slamming, resonators, wave attenuation, bandgap | | | | |
| 16. SECURITY CLASSIFICATION OF: | | | 17. LIMITATION OF ABSTRACT | 18. NUMBER OF PAGES 34 |
| a. REPORT UNCLASSIFIED | b. ABSTRACT UNCLASSIFIED | c. THIS PAGE UNCLASSIFIED | | |
| | | | | 19a. NAME OF RESPONSIBLE PERSON C. T. Sun 19b. TELEPHONE NUMBER (include area code) 765-494-5130 |

Final Report

Development of Toughened and Multifunctional Nanocomposites for Ship Structures

Prepared by

C.T. Sun
School of Aeronautics and Astronautics
Purdue University
West Lafayette, IN 47907

Submitted to
Office of Naval Research
One Liberty Center
875 North Randolph Street
Arlington, Virginia 22203

July 6, 2012

20120716098

Part I: Mechanical Properties of Fiber-Reinforced Composites with Silica Nanoparticle-Enhanced Matrix

OBJECTIVE

To achieve the benefit from adding nanoparticles to polymer matrix, the nanoparticles must be well dispersed in the matrix. Moreover, to maximize this benefit, high loading of nanoparticles must not cause adverse effects. The objective of the present research was to use a sol-gel in-situ produced silica nanoparticle-modified epoxy to manufacture fiber composites in order to enhance the mechanical properties of fiber composites. The corresponding theoretical models for strength and fracture toughness predictions were to be developed.

TECHNICAL APPROACH

An epoxy containing in-situ grown silica nanoparticles was used as the matrix to manufacture glass/epoxy composite. Vacuum assisted resin transfer molding (VARTM) process was used to fabricate unidirectional E-glass fiber reinforced silica/epoxy nanocomposites. Off-axis composite specimens with and without silica nanoparticles were tested to compare the compressive strength. A method for extracting the longitudinal compressive strength of the GFRP was developed based on the off-axis test data. Moreover, a microbuckling model was employed to predict the compressive strength based on the stress-strain curve of the silica nanocomposite.

ACCOMPLISHMENTS

1. Introduction

It is well known that most advanced fiber composites are stronger in tension (in the fiber direction) than in compression. This behavior is due to fact that the compressive strength of unidirectional composites is governed by microbuckling of fibers embedded in the matrix [1, 2]. It has been shown that composite compressive strength is proportional to the elastic-plastic tangent shear modulus of the matrix [3]. Thus, raising the elastic-plastic tangent shear modulus leads to a higher compressive strength of the composite.

It is now well established that the addition of a small amount of nanoparticles in a polymer may markedly improve its mechanical properties especially its stiffness. A few attempts have been made to take this advantage of nanoparticle infused matrix to enhance the compressive strength of composite [4-6]. Subramaniyan and Sun [4] reported about 17% and 19% gain in compressive elastic modulus with 3 wt% and 5 wt% nanoclay loadings, respectively, in vinyl ester resin. Using these stiffened matrices, they found about 22-36% improvement in the longitudinal compressive strength of glass fiber reinforced composite with 36% fiber volume fraction. Iwahori et al. [5] used 5-10 wt% cup-stacked type carbon nanofiber as reinforcing particles to stiffen epoxy matrix and reported 15% or less improvement in compressive strength of carbon/epoxy composite. On the other hand, Cho et al. [6] infused 3 wt% and 5 wt% disk-like graphite nanoparticles in epoxy via sonication and reported 10% and 16% gain in longitudinal compressive strength of carbon/epoxy composite respectively with 55% fiber volume fraction. Tsai and Wu [7] investigated the effect of nano-sized organoclay on tensile properties of glass fiber reinforced composites with particles loadings of 2.5-7.5 wt.%. They reported 74% and 67% improvement in transverse tensile strength and modulus whereas the properties deteriorated in the longitudinal direction. In all these studies, hand layup was used to fabricate the laminated composites and sonication was used to disperse nanoparticles in the resin (except [5]). These are the two major steps employed to produce fiber nanocomposites which are time and labor intensive and, thus, prevent bulk productions for real field applications. Moreover, with few exceptions, the mechanical properties (strength, fracture toughness) of nanocomposites produced

using these methods tend to go down when particle loading exceeds 4-5 wt% [8-10] due to poor dispersion of nanoparticles in the resin.

The main purpose of the present work is to verify that an epoxy containing well dispersed nanoparticles can be used to form fiber composites with a greatly enhanced compressive strength as well as tensile strength. Moreover, it is demonstrated that the more versatile VARTM process can be used to manufacture fiber composites with high nanoparticles loadings. In order to avoid the agglomeration of nanoparticles at higher loading, some researchers modified the chemical surface of the fillers to enhance the interfacial compatibility with the polymers— a process known as sol-gel. Using this method, organosol (colloidal fillers in organic solvent) is prepared with a required concentration, and then in the subsequent step, the solvent is replaced with polymers to form a well dispersed agglomerate-free nano-particle/polymer composite system. Several studies have been reported on silica /epoxy nanocomposites fabricated from organosilicasol [11-13]. Sprenger et al. [11] and Kinloch et al. [12] investigated the effect of silica nanoparticles on the fracture behavior of epoxy resin. However, in both cases, reactive liquid rubber (CTBN) was added as primary modifier to improve the fracture properties. The addition of silica nanoparticles further increased the toughness as well as retrieved the modulus loss due to the presence of flexible rubber molecules. Optimizing the epoxy with 6.9% CTBN and 3.5% silica, Sprenger et al. [11] made glass fiber reinforced composites and reported moderate increase (about 25%) in interlaminar fracture energy (G_{IC}) whereas Kinloch et al. [12] reported about 200% improvement in G_{IC} for carbon fiber reinforced composites. They added 9% CTBN and 10.5% silica to modify epoxy resin. While most of the works related to this material have focused on the fracture behavior [14-15], Zhang et al. [16] revealed 30-40% improvement in tensile and flexural modulus of epoxy resin with 23% silica.

In our previous study [17], we showed that flexural properties (strength, modulus) of silica/epoxy nanocomposite increased gradually with particle loading as contrast to the conventional one via sonication. The silica content was as high as 15% by weight. Adebahr et al. [18] showed the mechanical properties (toughness, modulus) can be improved with a particle loading upto 40 wt%. But the viscosity of silica/epoxy resin rose sharply after 15 wt% of silica content. In the present study, an epoxy with 15 wt% silica nanoparticles is used to fabricate glass fiber composite in order to be able to use the VARTM process. The VARTM process is slightly modified to make up for the increased viscosity of silica/epoxy resin. Compressive strengths of glass fiber composites with/without silica nanoparticles are measured using off-axis specimens. Tensile tests were also performed to evaluate longitudinal and transverse tensile strengths of nanocomposite. Finally, a microbuckling model is developed to predict the compressive strengths of the composites tested.

2. Experimental

2.1 Materials

The epoxy resin used in this study was diglycidylether of bisphenol A (DGEBA) with epoxy equivalent weight of 162 g/mole (SC 79 supplied by AP1 [19]) and the hardener was cycloaliphatic amine. The silica nanoparticles in epoxy (Nanopox F400) were procured from nanoresins AG [20]. The silica nanoparticles were synthesized from aqueous sodium silicate solutions by sol-gel technique [21]. After undergoing a process of surface modification and solvent exchange, the epoxy resin contains silica nanoparticles with an average particle size of 20 nm in diameter. Unidirectional E-glass fiber cloth (E-LR-0908-14) from Vectoreply® [22] was used to fabricate fiber reinforced laminates.

2.2 Fabrication

The required amount of Nanopox F400 was diluted with standard DGEBA to get 15 wt% of silica particles in the end product. In the subsequent step, the hardener was added and stirred

with a mechanical stirrer for about 5 minutes. In order to remove the bubbles produced during this vigorous mixing, the mixture was then degassed for an hour. After degassing, the mixture was poured into an aluminum mold and vitrified for 4 hours at a temperature of 60°C. The panel was then post cured.

Fiber reinforced composites were fabricated using VARTM process. A minor adjustment was made in VARTM process to make a continuous flow of nanophased epoxy (Nanopox F 400). Conventional VARTM procedures were followed for lay-up and arrangement of 16 layers of glass fibers with a vacuum pressure of 75 KPa. Usually, the air bubbles trapped in the resin and lay-ups are removed during this resin flow under vacuum. In case of the nanophased resin, it was not quite possible to completely take out the air bubbles due to the increased viscosity. Hence, the nanophased resin was degassed under vacuum for an hour before it was infused into the VARTM mold. For consistency, this step was also followed for neat resin. It should be noted that the nanophased resin flow time was as much as twice that of neat resin. The laminate was cured in hot press with a uniform pressure of 130 KPa under vacuum for about 4 hours at 60°C and then post-cured. Similar procedures were followed for tensile specimen by arranging 6 layers of glass fiber. For compression test specimens, composites with two fiber volume fractions of 42% and 50% were fabricated whereas it was 47% for tension test specimens.

2.3. Compression tests

2.3.1. Silica/epoxy resin

Block specimens (10mm×10mm×15mm) for the compression test were cut from neat and silica/epoxy matrix panels using a water jet cutting machine. All the specimens were then lapped with 6 μ m and 15 μ m diamond slurry to ensure parallel and smooth loading surfaces. Quasi-static compression tests were performed using an MTS machine with a self adjusting support (Fig. 1) to ensure uniform compressive pressure without any bending during the test. Lubricant was used on the contact surfaces between the specimens and the supports to minimize the contact friction to allow the induced shear deformation to fully develop during the test. The test was performed at a cross-head speed of 0.0015 mm/s with a nominal strain rate of 10^{-4} /s. Two strain gauges were mounted on two opposite sides of the specimen to monitor the bending of the specimen during the compression test.

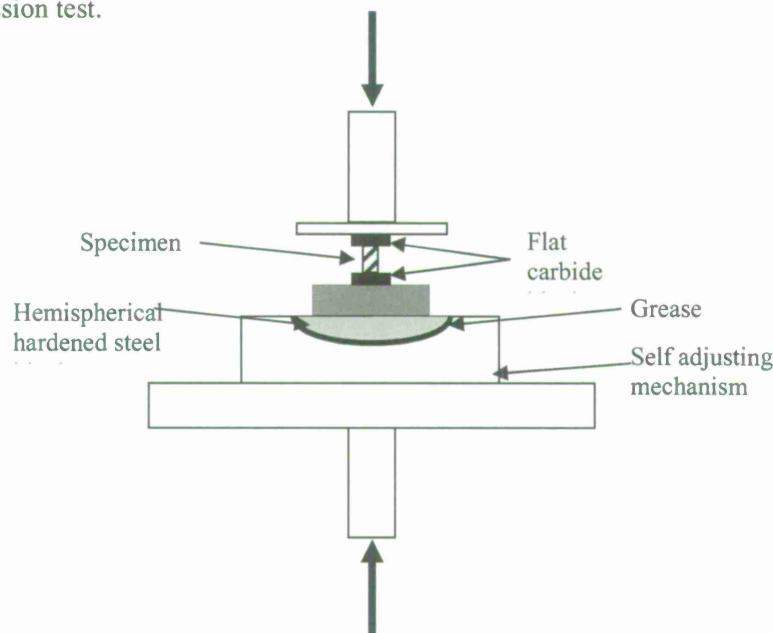


Figure 1: Self adjusting support for uniform

2.3.2. Fiber reinforced silica/epoxy nanocomposites

For unidirectional composites, compressive loading along the fiber direction (0°) often causes the failure in the form of fiber brooming which is an end failure and not a true representation of compressive strength of the composite. In this study, compression tests on off-axis composite specimens with angles of 5° , 10° and 15° were conducted from which the longitudinal compressive strength (0°) was extracted. The off-axis block specimen of $6\text{mm} \times 6\text{mm} \times 10\text{mm}$ were cut at these three angles from a unidirectional composite panel. Compression tests were performed at a cross head speed of 0.001 mm/s (Fig 1).

2.4 Tension tests

Tension tests were carried out in MTS machine in both longitudinal and transverse directions at a cross head speed of 1 mm/min . The longitudinal (0°) and transverse (90°) tension specimen dimensions were $230\text{mm} \times 12\text{mm} \times 2.2\text{mm}$ and $170\text{mm} \times 25\text{mm} \times 2.2\text{mm}$, respectively. 40 mm long PCB was used as the end-tabs, bonded using a high strength epoxy adhesive to prevent grip failure and slippage of specimens during the test.

3. Result and Discussion

3.1. Compressive properties of silica/epoxy resin

Silica/epoxy resin samples were imaged using a Phillips CM-100 TEM as shown in Fig. 2. The image shows a very uniform distribution of silica nanoparticles. The particles appear to be agglomeration-free and the individual particles can be identified very clearly.

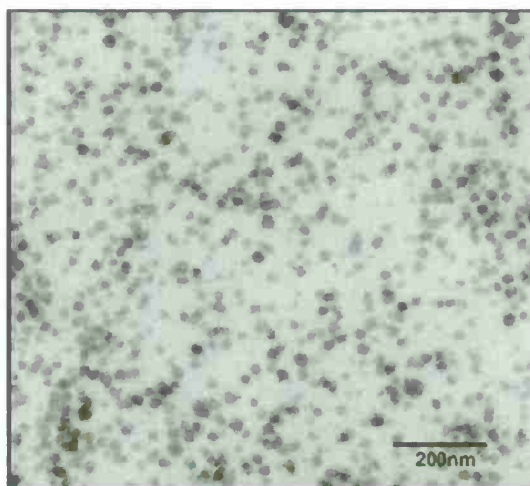


Figure 2: TEM images of 15 wt% silica/epoxy resin

Fig. 3 shows the compressive stress-strain curves of neat silica/epoxy resins. With 15 wt% silica nanoparticle loading, the Nanopox F400 nanocomposite shows a significant increase in compressive strength and modulus. The gain in compressive elastic modulus is about 40%. Similar improvements were reported in flexural strength, flexural modulus and failure strain with 15 wt% silica in epoxy fabricated from Nanopox F 400 [17]. It should be noted that the tangent modulus of the silica/epoxy is also higher than that of the neat epoxy.

3.2. Compressive strength of fiber reinforced nanocomposite

3.2.1. Off-axis compressive strength

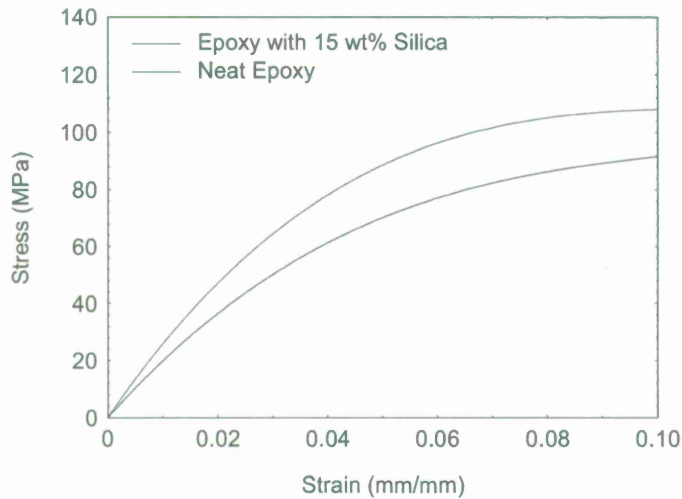


Figure 3: Compressive behaviors of neat and 15 wt% silica/epoxy resin

A typical microbuckling failure is shown in Fig. 4. The results of compressive strength are shown in Fig. 5 for three different off-axis angles of 5° , 10° and 15° . The figure shows the average values of at least 4 samples. Fig. 5 also shows the comparison of neat and nanophased composites with two fiber volume fractions (C_f) of about 42% and 50%, respectively. At all three off-axis angles, composites with the higher C_f show higher compressive strengths than those of composites with the lower C_f for both neat and nanophased composites. The low C_f nanophased composites show 10-30% improvement in strength than the neat composite at corresponding angles. However, the improvement is much pronounced (20%-40%) in high C_f composites than the low C_f composites.

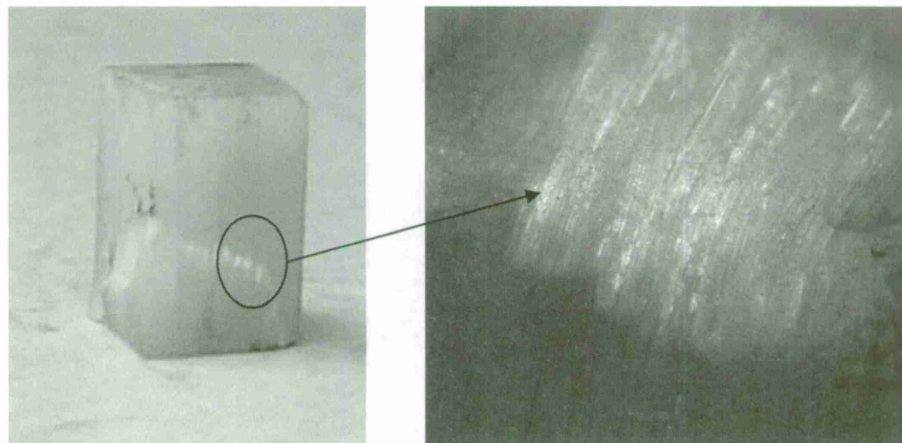


Figure 4: Typical microbuckling failure

3.2.2. Longitudinal compressive strength

Theoretically, the longitudinal compressive strength of a unidirectional fiber composite can be measured by conducting a compression test on the 0° specimen. However, such a test often produces end (brooming) failure rather than microbuckling failure. Lee and Soutis [23] conducted compression tests in combined shear loading and end loading by employing an anti-buckling device. Their test results showed a decreased compressive strength of unidirectional

composites as specimen thickness increased, and observed end failures in thick-section composite specimens. In most of the studies in compressive strength of composites, shear loading through the use of end tabs or wedge grips was utilized partially or fully in conducting compression tests. Thus, the compressive strengths measured were influenced by the presence of shear stresses.

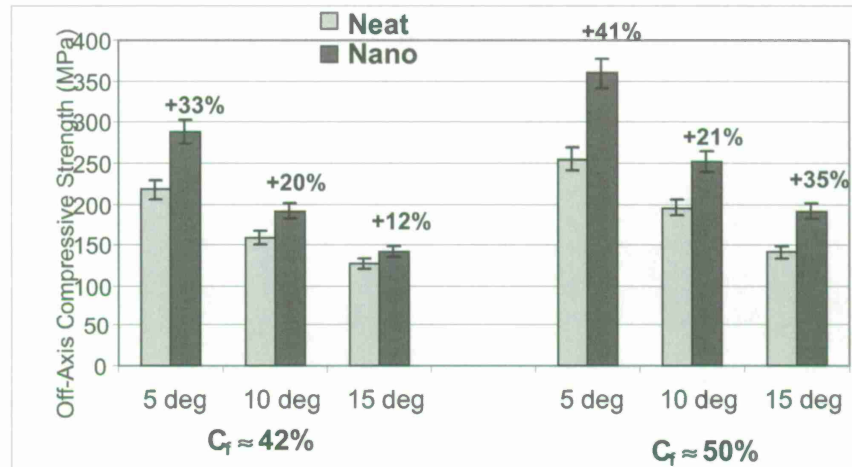


Figure 5: Off-axis compressive strengths of neat and nanophased fiber composites

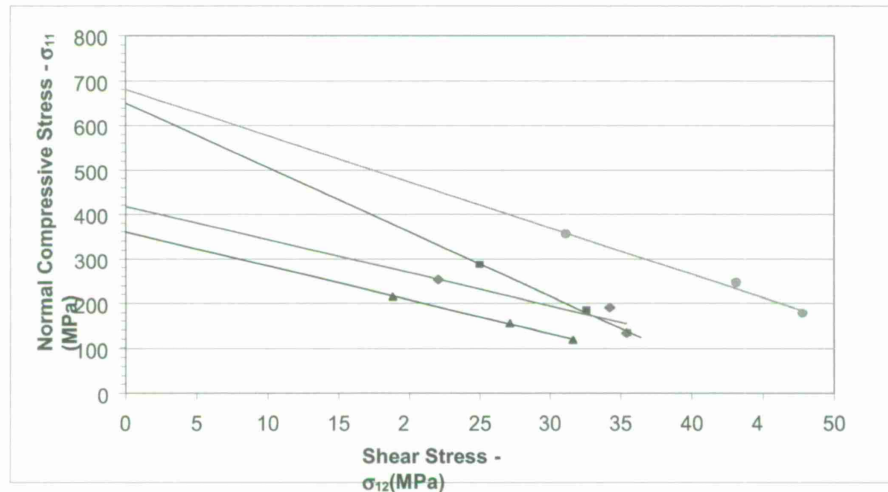


Figure 6: Extraction of longitudinal compressive strengths of neat and nanophased fiber composites

In this study, the longitudinal compressive strength was extracted from off-axis strength results by extrapolation and by the elastic-plastic fiber microbuckling model. The applied compressive strength on the off-axis specimen is first transformed into normal stress σ_{11} and shear stress σ_{12} (according to the coordinate transformation law) and then plotted for fiber composites containing neat and nanophased matrices with fiber volume fractions of 42% and 50%, respectively, as shown in Fig. 6. The longitudinal compressive strength corresponds to the value of σ_{11} at $\sigma_{12} = 0$, i.e., the 0 degree specimen. According to the fiber microbuckling model to be presented in Section 4, compressive strength is not linearly dependent on shear stress. However, from Fig. 6, for each composite system a straight line seems to give a good fit of the off-axis

strength data. Thus, the longitudinal strength for each composite system is extracted based on this linear projection. This projection technique has been used elsewhere with fairly good results as compared with experimental data or model predictions [4, 24]. The composite compressive strengths obtained in this manner are tabulated in Table 1, which indicate 81% and 62% improvements in longitudinal compressive strength for composites with 15 wt% silica particles for 42% and 50% fiber volume fractions, respectively.

Table 1: Longitudinal compressive strengths of neat and nanophased fiber composites

| Fiber Volume Fraction | Longitudinal Compressive Strength (MPa) | | Improvement |
|-----------------------|---|------|-------------|
| | Neat | Nano | |
| $\approx 42\%$ | 360 | 650 | 81% |
| $\approx 50\%$ | 420 | 680 | 62% |

3.3 Tensile strength of fiber reinforced nanocomposite

3.3.1 Longitudinal tensile strength

The respective average values of tensile strength and Young's modulus of composites with/without silica nanoparticles are shown in Fig. 7. It was found that silica nanoparticles yield little effect on the Young's modulus of the nanocomposite. This is expected because matrix modifications, in general, would not influence fiber dominated properties. However, it is interesting to find that the nanocomposite with 15wt% spherically shaped silica nanoparticles showed 11% increase in longitudinal tensile strength. The addition of well dispersed silica nanoparticles reduces the brittleness of epoxy matrix [17] and, as a result, may attribute to the slight increase in longitudinal tensile strength.

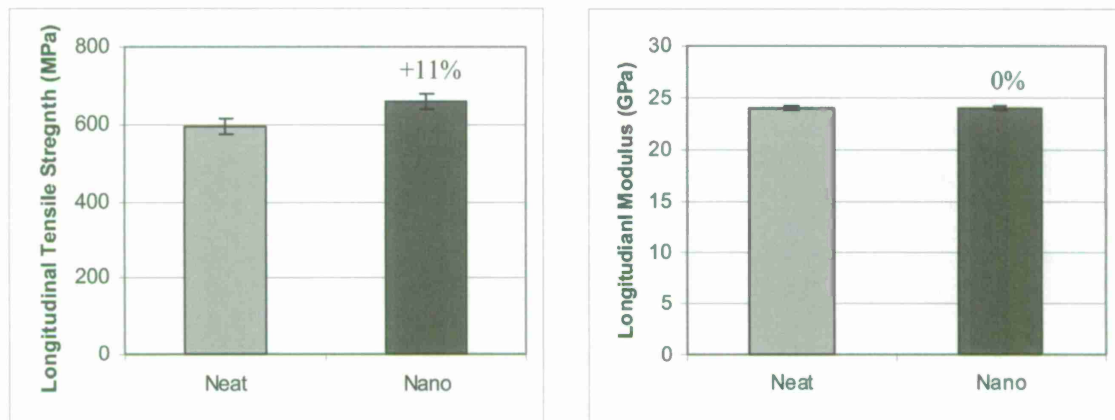


Figure 7: Tensile strength and modulus in longitudinal direction

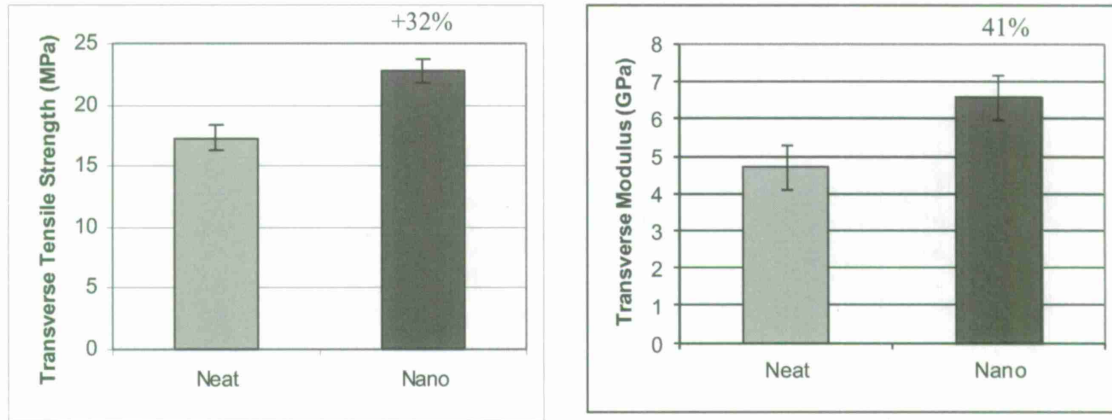


Figure 8: Tensile strength and modulus in transverse direction

3.3.2 Transverse tensile strength

The average transverse tensile strengths and moduli of composites with/without silica nanoparticles are shown in Fig. 8. It was found that the nanocomposite shows 32% and 41% increase in tensile strength and modulus in the transverse direction, respectively. For transversely loaded tension specimens, matrix cracking is the dominant failure mode for unidirectional composites. Hence, the improvement in the transverse tensile strength of the nanocomposite may be attributed to stiffened matrix due to the addition of nanoparticles.

4. Prediction by Microbuckling Model

An existing fiber microbuckling model developed by Sun and Jun [3] is used to validate the longitudinal compressive strength of both neat and nanophased unidirectional composites as discussed in Section 3.2.2. Sun and Jun [3] developed this model based on Rosen's [2] elastic microbuckling model and obtained the longitudinal compressive strength for unidirectional fiber composites as

$$\sigma_c = \frac{G_m^{ep}}{1 - C_f} \quad (1)$$

where C_f is the fiber volume fraction and G_m^{ep} is the matrix elastic-plastic tangent shear modulus. Details of the derivation can be found in Ref.3. This compression failure model was later extended by Subramaniyan and Sun [4] for large off-axis angles.

From Sun and Jun model [3], the incremental plastic shear strain in the matrix is obtained as

$$d\gamma_{12}^p = \frac{9\sigma_{12}^2}{H_p \bar{\sigma}^2} d\sigma_{12} \quad (2)$$

where $H_p = \frac{d\bar{\sigma}}{d\bar{\epsilon}_p}$ is the plastic tangent modulus which depends on the instantaneous state of stress. The effective stress $\bar{\sigma}$, the effective stress increment $d\bar{\sigma}$, and the effective plastic strain increment $d\bar{\epsilon}_p$ can be expressed as

$$\begin{aligned} \bar{\sigma} &= \sqrt{3J_2} = \sigma \sqrt{\beta^2 \cos^4 \theta + 3 \sin^2 \theta \cos^2 \theta} \\ d\bar{\sigma} &= d\sigma \sqrt{\beta^2 \cos^4 \theta + 3 \sin^2 \theta \cos^2 \theta} \\ d\bar{\epsilon}_p &= \sqrt{\frac{2}{3}} d\epsilon_{ij}^p d\epsilon_{ij}^p \end{aligned}$$

where $\beta = \frac{1}{\alpha C_f + C_m}$, $\alpha = \frac{E_f}{E_{ms}}$, C_m is the matrix volume fraction, E_f is the fiber modulus, θ is the off-axis angle, and E_{ms} is the secant modulus of the matrix calculated from the uniaxial stress strain curve of the matrix.

By using $\sigma_{12} = \sigma \sin \theta \cos \theta$, the plastic shear strain increment given in eqn. 2 can be written as $d\gamma_{12}^p = \frac{9 \sin^2 \theta}{(\beta^2 \cos^2 \theta + 3 \sin^2 \theta) H_p} d\sigma_{12}$. The elastic shear strain increment is given by

$d\gamma_{12}^e = \frac{d\sigma_{12}}{G_m}$ where G_m is the elastic shear modulus of the matrix. After adding the elastic and plastic shear strain increments and rearranging, the matrix elastic-plastic shear modulus can be expressed as

$$G_m^{ep} = \left[\frac{1}{G_m} + \frac{9 \sin^2 \theta}{(\beta^2 \cos^2 \theta + 3 \sin^2 \theta) H_p} \right]^{-1} \quad (3)$$

As the matrix elastic-plastic tangent shear modulus depends on stresses at the time of microbuckling, eqn. 1 must be solved numerically. An incremental procedure is used to find the critical compressive strengths at different off-axis angles as well as 0° . The composite applied stress σ is increased incrementally from zero and the initial value of α was calculated. At each stage, β and effective stress $\bar{\sigma}$ in the matrix are calculated. The effective plastic strain $\bar{\epsilon}_p$ corresponding to this effective stress $\bar{\sigma}$ is found from the effective stress-effective plastic strain curve which is the same as the uniaxial stress/plastic strain curve of the matrix. In the next step, the effective stress increment $d\bar{\sigma}$ and the effective plastic strain increment $d\bar{\epsilon}_p$ are also calculated from which the plastic tangent modulus H_p is obtained. The secant modulus E_{ms} is also calculated from current effective stress-effective plastic strain curve and is used to find α for next step. Once H_p is known, eqn. 3 is used to find the elastic-plastic shear modulus of the matrix and eventually the current critical stress in the composite is obtained. The process is repeated until the critical stress exceeded the applied stress and hence giving the composite failure stress.

The experimental compressive failure stresses for different off-axis angles are shown in Fig. 9. The model predictions are also presented as solid lines. The initial fiber misalignment angles are chosen to fit the experimental data. The misalignment angles vary between $2-3.6^\circ$ for different composite panels and are shown in Table 2. However, these values are within the experimental measurements of fiber misalignment of composites [25]. Except for the nanocomposite with 49% fiber volume, the model predictions agree quite well with the experimental results.

Table 2: Misalignment angles for different composites

| Type | Volume Fraction | Misalignment Angle |
|------|-----------------|--------------------|
| Neat | 43% | 3.4 |
| | 50% | 3 |
| Nano | 42% | 2.6 |
| | 49% | 2 |

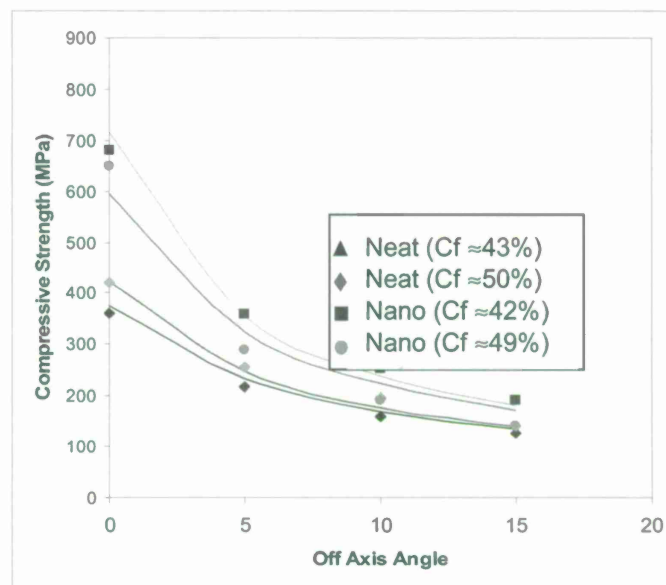


Figure 9: Prediction of compressive strength using microbuckling model

5. Conclusion

It is concluded that sol-gel is a very effective method for producing agglomerate-free silica nanoparticles in epoxy resins. With 15 wt% silica nanoparticle loading, the nanophased resin showed a greater elastic modulus than that of the neat resin. The silica-nanoparticle modified resin (Nanopox F 400) substantially enhanced the longitudinal compressive strength of E-glass fiber reinforced composites. It was found that the enhancement was greater in fiber composites with lower fiber volume fractions. In case of tensile properties, the composite with silica nanoparticles-enhanced matrix showed a slight improvement in the longitudinal direction whereas the improvement in the transverse direction was quite significant. The elastic-plastic microbuckling model can be used to predict the enhancement in the composite compressive strength based on the stress-strain curve of the modified matrix.

It has been demonstrated that the VARTM process with a minor adjustment can be used to manufacture quality nanocomposites even with high (15 wt%) particle loadings. Due to the small size (20nm) of the silica particle and its spherical shape, the filtration of particles during the VARTM process was avoided. Moreover, the silica nanoparticles were grown in-situ using the sol-gel method which can be readily produced in bulk. The proposed method of making fiber reinforced composites with silica nanoparticle-modified epoxy matrix appears to be feasible for volume productions.

6. References

1. Dow N F and Gruntfest I J. Determination of Most Needed Potentially Possible Improvements in Materials for Ballistic and Space Vehicles. GE-TIS. 1960;60: 389.
2. Rosen B W. Mechanics of Composite Strengthening. Fiber Composite Materials, American Society Metals Seminar 1965.
3. Sun C T and Jun A W. Compressive Strength of Unidirectional Fiber Composites with Matrix Non-linearity. Comp Sci and Tech 1994; 52: 577.
4. Subramaniyan A K and Sun CT. Enhancing Compressive Strength of Unidirectional Polymeric Composites using Nanoclay. Composites Part A 2006; 37(12): 2257.

5. Iwahori Y, Ishiwata S, Sumizawa T and Ishikawa T. Mechanical Properties Improvements in Two-Phase and Three-Phase Composites using Carbon Nano-fiber Dispersed Resin. *Composites Part A* 2005; 36: 1430.
6. Cho J, Chen J Y and Daniel I M. Mechanical Enhancement of Carbon Fiber/Epoxy Composites by Graphite Nanoplatelet Reinforcement. *Scripta Mater* 2007; 56: 685.
7. Tsai, J. L. and Wu, M. D. Organoclay Effect on Mechanical Responses of Glass/Epoxy Nanocomposites. *J of Comp. Mater.* 2007; 41 (20): 2513.
8. Zheng Y, Ning R and Zheng Y. Study of SiO₂ Nanoparticles on the Improved Performance of Epoxy and Fiber Composites. *J of Reinf. Plast. Comp* 2005; 24:223.
9. Rodgers R M, Mahfuz H, Rangari V K, Chisholm N and Jeelani S. Infusion of SiC Nanoparticles into SC-15 Epoxy: An Investigation of Thermal and Mechanical Response. *Macromol. Mater. Eng* 2005; 290: 423.
10. Choi Y-K, Sugimoto K, Song S, Gotoh Y, Ohkoshi Y and Endo M. Mechanical and Physical Properties of Epoxy Composites Reinforced by Vapor Grown Carbon Nanofibers. *Carbon* 2005; 43: 2199.
11. Sprenger S, Kinloch A J, Taylor A C and Mohammed R D. Rubber-Toughened GFRCs Optimised by Nanoparticles. *J of European Coating* 2005; 21: 66.
12. Kinloch A J, Mohammed R D, Taylor A C, Sprenger S and Egan D. The Interlaminar Toughness of Carbon-Fibre Reinforced Plastic Composites using 'Hybrid-Toughened' Matrices. *J of Mat. Sci., Letter* 2006; 41: 5043.
13. Sprenger S, Kinloch A J, Taylor A C and Mohammed R D. Rubber-Toughened CFRCs Optimised by Nanoparticles -Part III. *J. of European Coating* 2007; 30: 54.
14. Kinloch A J, Mohammed R D and Taylor A C. The Effect of Silica Nano Particles and Rubber Particles on the toughness of Multiphase Thermosetting Epoxy Polymers. *J of Mat Sci, Letters* 2005.
15. Kinloch A J, Lee J H, Taylor A C, Sprenger S, Eger C and Egan D. Toughening Structural Adhesives Via Nano and Micro Phase Inclusions. *J. Adhes.* 2003; 79: 867.
16. Zhang H, Zhang Z, Friedrich K and Eger C. Property Improvements of an in Situ Epoxy Nanocomposites with Reduced Interparticle Distance at High Nanosilica Content. *Acta Mater* 2006; 54: 1833.
17. Uddin M F and Sun C T. A New Processing Method for High Particle Loading Silica/Alumina/Epoxy Hybrid Nanocomposites. *Proceedings of the Twelfth U.S.-Japan Conference on Composite Materials* 21-22 September, 2006; 49.
18. Adebhar T, Roscher C and Adam J. Reinforcing Nanoparticles in Reactive Resins. *European Coatings Journal* 2001; 4: 144.
19. Applied Poleramic Inc. 6166 Egert Court, Benicia, CA 94510.
20. nanoresins AG. Charlottenburger Str. 9 21502 Gecsthacht, Germany.
21. Adam, J. Silicon Dioxide Dispersion. US Patent 20040147029 (WO 02083776).
22. Vectorply Corporation. 3500 Lakewood Drive, Phoenix City, AL 36867, USA.
23. Lee J, Soutis C. Thickness Effect on the Compressive Strength of T800/924C Carbon Fibre-epoxy Laminates. *Compos Part A* 2005; 36(2): 213.
24. Tsai J and Sun C T. Dynamic Compressive Strengths of Polymeric Composites. *Intl. J Solid Struet.* 2004; 41: 3211.
25. Yurgartis S W. Measurement of Small Angle Fiber Misalignment in Continuous Fiber Composites. *Comp Sci Tech* 1987; 30(4): 279.

Part II: Novel Sandwich Structures with Internal Resonators

OBJECTIVE

The objective of this study is to investigate the dynamic behavior of sandwich structures containing a novel core with embedded resonators. By designing the resonance frequency of the resonators, the sandwich structure is expected to reject impinging waves. If successfully completed, this type of sandwich structures will become quiet under dynamic loads.

TECHNICAL APPROACH

In a typical sandwich construction, the face sheets are the major load-bearing components and the lightweight core is used to support the face sheets and take the transverse shear force. A weakness of sandwich structures is their low impact resistant strength and impact energy absorption capability. We propose to add a very important function in the core for blocking incident blast wave and increasing its capability in storing temporarily the impact energy. Resonators are inserted into the core to provide a new degree of freedom in motion. Models for this new sandwich structure are first constructed. These models are subsequently employed to study wave propagation in and the bandgap structure of the sandwich structure. Finally, sandwich specimens are manufactured and dynamic experiments are conducted to verify the analytical results.

ACCOMPLISHMENTS

1. Introduction

In a typical sandwich construction, the face sheets are the major load-bearing components and the lightweight core is used to support the face sheets and take the transverse shear force. A weakness of sandwich structures is their low impact resistant strength and impact energy absorption capability. In the present study, we propose to add a very important function in the core for blocking incident blast wave and increasing the capability in storing temporarily the impact energy. Figure 1 shows a design of such a sandwich construction with a foam core that contains distributed “rigid” containers that are embedded in the foam core. Inside each container there is an internal mass/resonator supported by a spring.

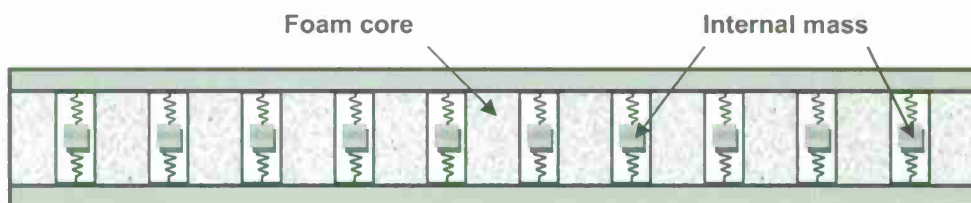


Figure 1 Sandwich beam with internal resonators.

In the sandwich beam, each resonator consists of a mass m and a linear spring with a spring constant denoted by k . By employing an energy averaging technique, the deformation energy and kinetic energy per unit length for the sandwich beam are obtained as

$$U = \frac{1}{2} \left\{ EI \left(\frac{\partial \varphi}{\partial x} \right)^2 + GA \left(\frac{\partial v}{\partial x} + \varphi \right)^2 \right\} + \frac{1}{2} \frac{k}{a} (v_1 - v)^2 \quad (1)$$

$$T = \frac{1}{2} (\rho A \dot{v}^2 + \rho I \dot{\varphi}^2) + \frac{1}{2} \frac{m}{a} \dot{v}_1^2 \quad (2)$$

respectively, where GA is transverse shear rigidity, EI is bending rigidity, ρA is mass of the sandwich beam per unit length, ρI is rotary inertia, v and φ are the transverse displacement and rotation of the sandwich beam, respectively, v_1 is the transverse displacement of the internal mass, and a is the spacing of the internal masses. By using the Hamilton's principle, the equations of motion for the sandwich beam are obtained as

$$\begin{aligned} GA(v'' + \varphi') - \rho A \ddot{v} + \frac{k}{a} (v_1 - v) &= 0 \\ EI \varphi'' - GA(v' + \varphi) - \rho I \ddot{\varphi} &= 0 \\ \frac{k}{a} (v_1 - v) + \frac{m}{a} \ddot{v}_1 &= 0 \end{aligned} \quad (3)$$

2. Dispersion curves

For harmonic waves, the three displacement functions v , φ , and v_1 all contain the wave form $e^{i(qx - \omega t)}$ in which q is wave number and ω is angular frequency. The dispersion equation can be readily obtained as

$$A_1 \omega^6 + A_2 \omega^4 + A_3 \omega^2 + A_4 = 0 \quad (4)$$

where

$$\begin{aligned} A_1 &= -\rho I \rho A \left(\frac{m}{a} \right), \\ A_2 &= \left\{ (\rho I GA + EI \rho A) \left(\frac{m}{a} \right) q^2 + GA \rho A \left(\frac{m}{a} \right) + \rho I \rho A \left(\frac{k}{a} \right) + \left(\frac{km}{a^2} \right) \rho I \right\}, \\ A_3 &= - \left\{ EIGA \left(\frac{m}{a} \right) q^4 + \left\{ (\rho I GA + EI \rho A) \left(\frac{k}{a} \right) + \left(\frac{km}{a^2} \right) EI \right\} q^2 + GA \rho A \left(\frac{k}{a} \right) \right. \\ &\quad \left. + \left(\frac{km}{a^2} \right) GA \right\}, \quad A_4 = EIGA \left(\frac{k}{a} \right) q^4. \end{aligned}$$

Figure 2 shows the three branches of the dispersion curves of harmonic waves propagating in a sandwich beam of infinite extent. The dimensions and material parameters adopted in the

calculations are listed in Table 1. The face sheets are IM7/953-2A $[0/90]_{25}$ laminates with an effective elastic modulus E_f ; the core material is Rohacell IG-3 with elastic shear modulus G_c . The thicknesses of the sheet and the core are denoted by h_f and h_c , respectively, and b denotes the width of the beam. The densities of the face sheet and the core are 1600 kg/m^3 and 32 kg/m^3 , respectively. Table 2 summarizes the bending rigidity, shear stiffness, mass per unit length, and rotary inertia of the sandwich beam. The accuracy of the present sandwich beam model is evaluated by comparing the results obtained from theoretical model given by equation (4) with those obtained by a finite element analysis based on the original discrete mass model.

Table 1 Dimension and material constants of the face feet and the core.

| $E_f(\text{GPa})$ | $G_c(\text{MPa})$ | $h_f(\text{m})$ | $h_c(\text{m})$ | $b(\text{m})$ | $a(\text{m})$ | $k(\text{N/m})$ | $m(\text{kg})$ |
|-------------------|-------------------|-----------------|-----------------|---------------|---------------|-----------------|----------------|
| 92 | 10 | 0.001 | 0.025 | 0.025 | 0.01 | 10^3 | 10^{-2} |

Table 2 Properties of the sandwich beam.

| $EI(\text{Pa} \cdot \text{m}^4)$ | $GA(\text{Pa} \cdot \text{m}^2)$ | $\rho A(\text{kg/m})$ | $\rho I(\text{kg} \cdot \text{m})$ |
|----------------------------------|----------------------------------|-----------------------|------------------------------------|
| 776.25 | 6.75×10^3 | 0.1 | 1.4542×10^{-5} |

In Figure 2, the normalized angular frequency is defined as $\bar{\omega} = \omega/\omega_0$ where $\omega_0 = \sqrt{k/m} = 316 \text{ rad/sec}$ is the local resonance frequency of the resonator, and $\bar{q} = qa$ is dimensionless wave number. It is noted that there is a band gap between $\bar{\omega} = 1$ and $\bar{\omega} = 3.317$. Theoretically, in this frequency range, harmonic waves cannot propagate. The aforementioned phenomenon may be explained more explicitly by investigating the nature of the dimensionless wave number for wave frequencies within the band gap. For this purpose, the dispersion equation, equation (4), can be viewed as an equation for wave number q as a function of frequency ω . For a given frequency ω the solution for wave number can be calculated from equation (4). The solution may be complex in the form of $\bar{q} = aq = \alpha + i\beta$. If β exists, then the wave amplitude should exhibit a spatial decay. This is why β is referred to as "attenuation factor." Of interest is that when wave frequency approaches the local resonance frequency ω_0 , the attenuation factor β becomes unbounded. In other words, the maximum wave attenuation would be attained at the local resonance.

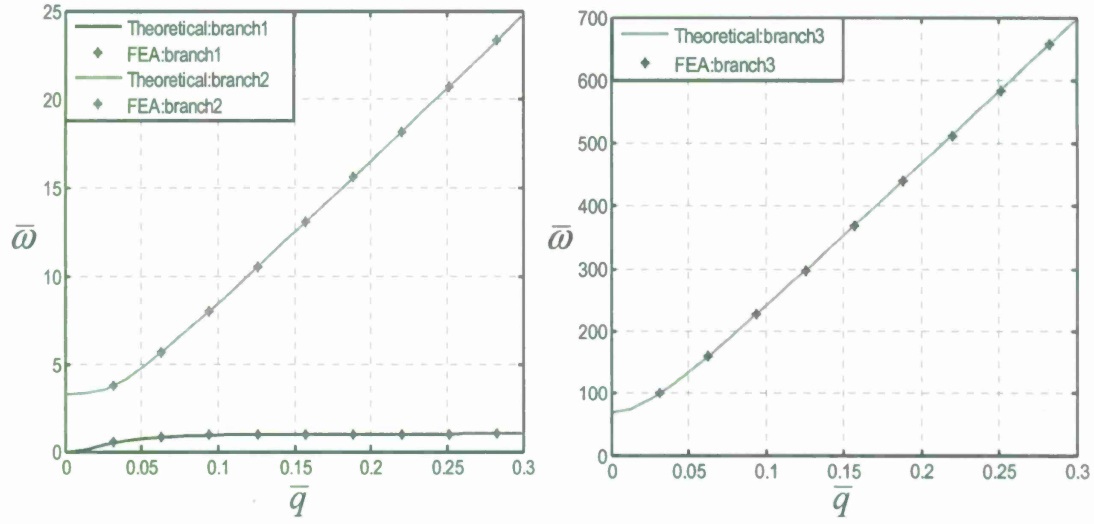


Figure 2 Dispersion curves for harmonic waves: three branches.

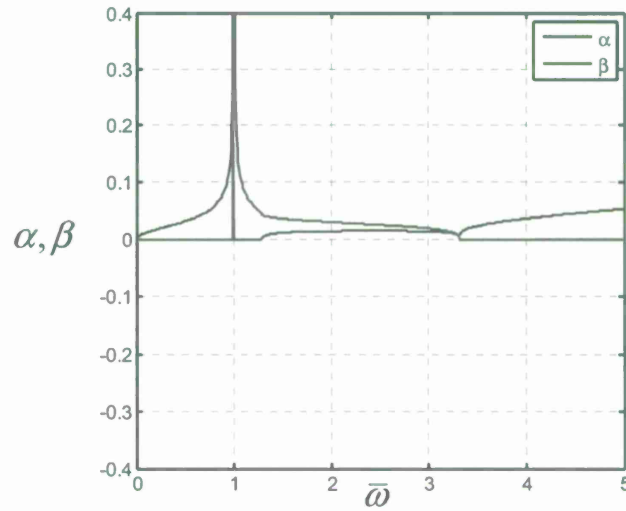


Figure 3 Attenuation factor as a function of dimensionless frequency $\bar{\omega}$.

3. Continuum Representation

If the sandwich beam with internal resonators is treated as a conventional sandwich beam with an effective core, then the equations of motion reduce to

$$\begin{aligned} GA(v'' + \phi') - (\rho A)_{\text{eff}} \ddot{v} &= 0 \\ EI\phi'' - GA(v' + \phi) - \rho I \ddot{\phi} &= 0 \end{aligned} \quad (5)$$

in which $(\rho A)_{eff}$ is the effective mass per unit length. The dispersion equation based on this model can be expressed as

$$GA EI q^4 - (GA \rho I \omega^2 + EI (\rho A)_{eff} \omega^2) q^2 + (\rho I \omega^2 - GA) (\rho A)_{eff} \omega^2 = 0 \quad (6)$$

To truly represent the original sandwich beam with resonators, the equivalent mass $(\rho A)_{eff}$ of this representative sandwich beam has to be chosen so that the dispersion curves match those of the exact ones presented in figure 2. The result is

$$(\rho A)_{eff} = \frac{GA \rho I \omega^2 - GA EI q^4}{\{\rho I \omega^2 - GA - EI q^2\} \omega^2} \quad (7)$$

Since the dispersion curves obtained from equation (4) give the solution of q^2 in terms of frequency ω , thus, $(\rho A)_{eff}$ can be considered as a function of frequency alone. Consequently, the dimensionless frequency-dependent mass per unit length $(\rho A)_{eff} / \rho A$ can be depicted as a function of frequency as shown in figure 4. It is seen that when wave frequency approaches the local resonance (*i.e.*, $\bar{\omega} \rightarrow 1$), the effective mass becomes unbounded. Moreover, the effective mass becomes negative if $\bar{\omega} > 1$. In fact, the frequency region of negative effective mass coincides with the band gap.

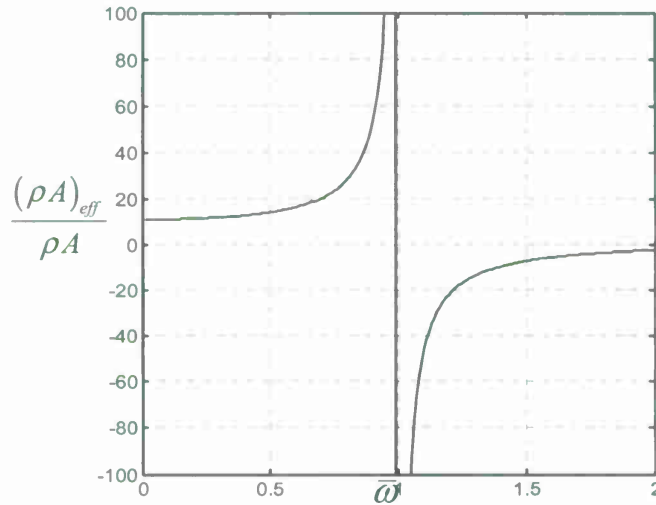


Figure 4 Dimensionless effective mass per unit length.

4. Transient Response

Consider a long sandwich beam with resonators as shown in figure 1. The left end is assumed to be actuated with a prescribed displacement given by

$$\begin{aligned} v(t) &= v_0 \sin \omega t & t \geq 0 \\ v(t) &= 0 & t \leq 0 \end{aligned} \quad (8)$$

The corresponding frequency spectrum of the actuation for $\omega = 319.4$ rad/sec (or $\omega/\omega_0 = 1.01$) is shown in figure 5. It is evident that the dominant forcing frequency is $\omega = 319.4$ rad/sec. The deformed shape of the first 4 m of the sandwich beam at time 0.439 sec is displayed in figure 6(a). Figure 6(b) shows the snap shot of the vertical motions of the internal masses at time 0.439 sec. The results of figures 6(a) and 6(b) clearly show a significant spatial decay of amplitude of the flexural motion of the beam. In other words, the motion produced by the actuation at the left end is forbidden to propagate into the sandwich beam. It is also noted that the amplitude of vibration of the internal masses is more than an order of magnitude larger than that of the sandwich beam. This indicates that a much greater portion of the actuation work is stored in the resonators especially in those near the actuated end.

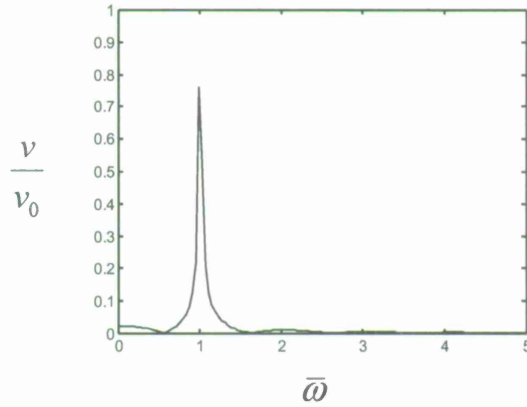


Figure 5 Frequency spectrum of the displacement actuation.

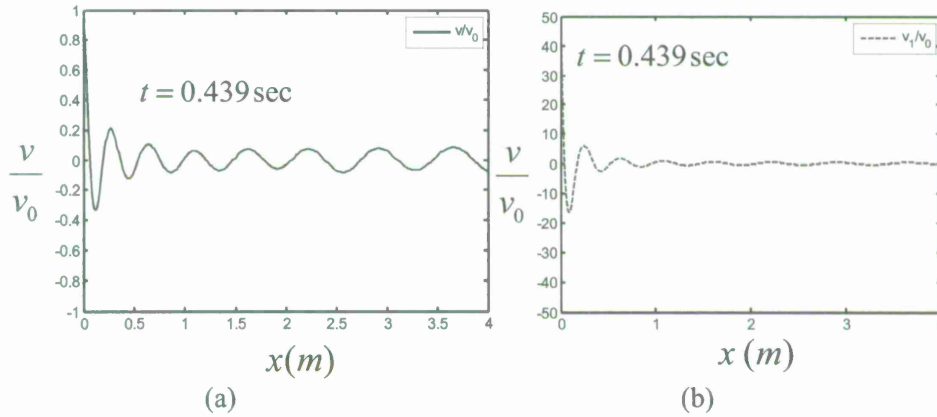


Figure 6 Mode shape at time 0.439 sec for (a) sandwich beam deflection v and (b) displacements of the resonators.

5. Experimental Verification

In the previous sections, the behavior of wave propagation in a sandwich beam with internal resonators was studied analytically. It was found that, with the occurrence of a bandgap,

waves generated by actuations in certain frequency range were forbidden to propagate into the sandwich beam without attenuation. By tailoring the local resonance frequency of the resonator, the range and the location of the bandgap can be selected. Also, from finite element simulation results, it was seen that waves could be significantly attenuated in a sandwich beam with a finite number of internal resonators if the forcing frequency was near the local resonance frequency. It was concluded that the resonators could be used as a mechanism for suppressing the flexural motion in a sandwich structure. In this section, experimental results are presented.

5.1 Specimen and Experimental Set-up

In order to verify the analytical as well as numerical results, a sandwich beam of rectangular cross-section 1.905×3.175 cm and 75.7 cm long was fabricated. The core consists of Rohacell IG-51 foam with 61 holes drilled through the thickness periodically to accommodate resonators. A representative individual resonating element is shown in Fig. 7. Empty plastic tubes were inserted in the first 14.5 cm, plastic tubes containing the spring-mass system (resonating units) were inserted in the next 31.4 cm and again empty plastic tubes without resonators were inserted in the remaining length of the beam. The face sheets used are AS4/3501-6 composite laminates with stacking sequence $[0_2/90_2/0_2]$. A schematic of the beam is shown in Fig. 8. For comparison, another sandwich beam without the resonators was also fabricated.



Fig. 7 Individual spring-mass-spring and an assembled unit cell.

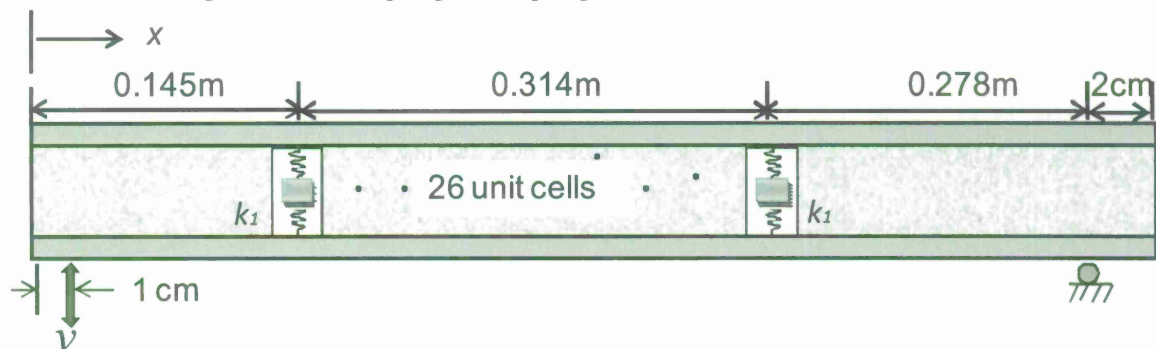


Fig. 8 Sandwich beam having a section with resonators.

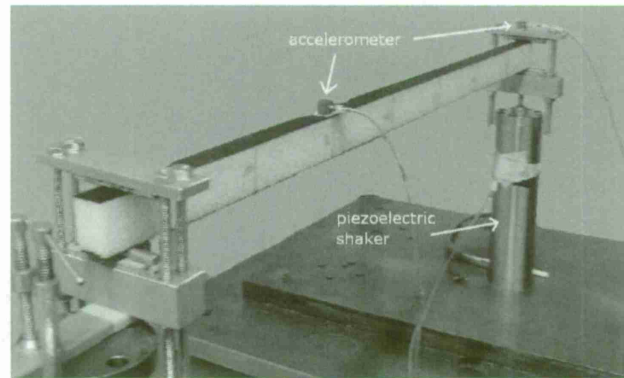


Fig. 9 Experimental set-up.

Figure 9 shows the experimental set-up. The sandwich beam was simply supported on one end while the other end excited by a piezoelectric stack actuator. The stack actuator used was model PSt 1000/25/200, obtained from Piezomechanik GmbH. The power for the Piezostack operation came from a complimentary Piezomechanik GmbH high power amplifier (model RCV 1000/5). The shaker provides the input excitation generated using a waveform generator.

5.2 Experimental Results

Wave bandgaps are effectively described using the frequency response function (FRF) [1]. For comparison, the FRFs for the beams with and without the resonators were acquired using a white-noise signal with bandwidth from 0 to 1000Hz. The input was obtained by a force transducer attached at the input end, while the output acceleration was measured 60 cm away from the input end. The obtained FRFs are shown in Fig. 10. A clear dip in the FRF corresponding to the local resonance frequency is seen for the beam with resonators, while no such a bandgap is found in the FRF for the beam without resonators. Also, the modal peaks in the beam with resonators are shifted to lower frequencies due to the added mass in the beam.

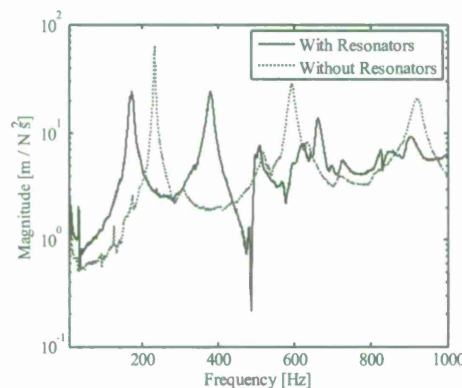


Fig. 10. Comparison of frequency responses of beams with and without resonators to noise i/p.

Moreover, displacement time histories at various fixed frequencies were measured using B&K 4507B accelerometers. One accelerometer was placed at the point of excitation to estimate the input displacement history, while the second accelerometer was placed at the output end. The collected accelerometer signals were numerically integrated twice to obtain the displacement history. The displacement time-histories obtained at the specified locations at a driving frequency of 497Hz are shown in Fig. 11. The results obtained show a substantial amplitude decay of the flexural motion of the beam with resonators as compared to that of the beam without resonators

when driven at a frequency close to the local resonance frequency.

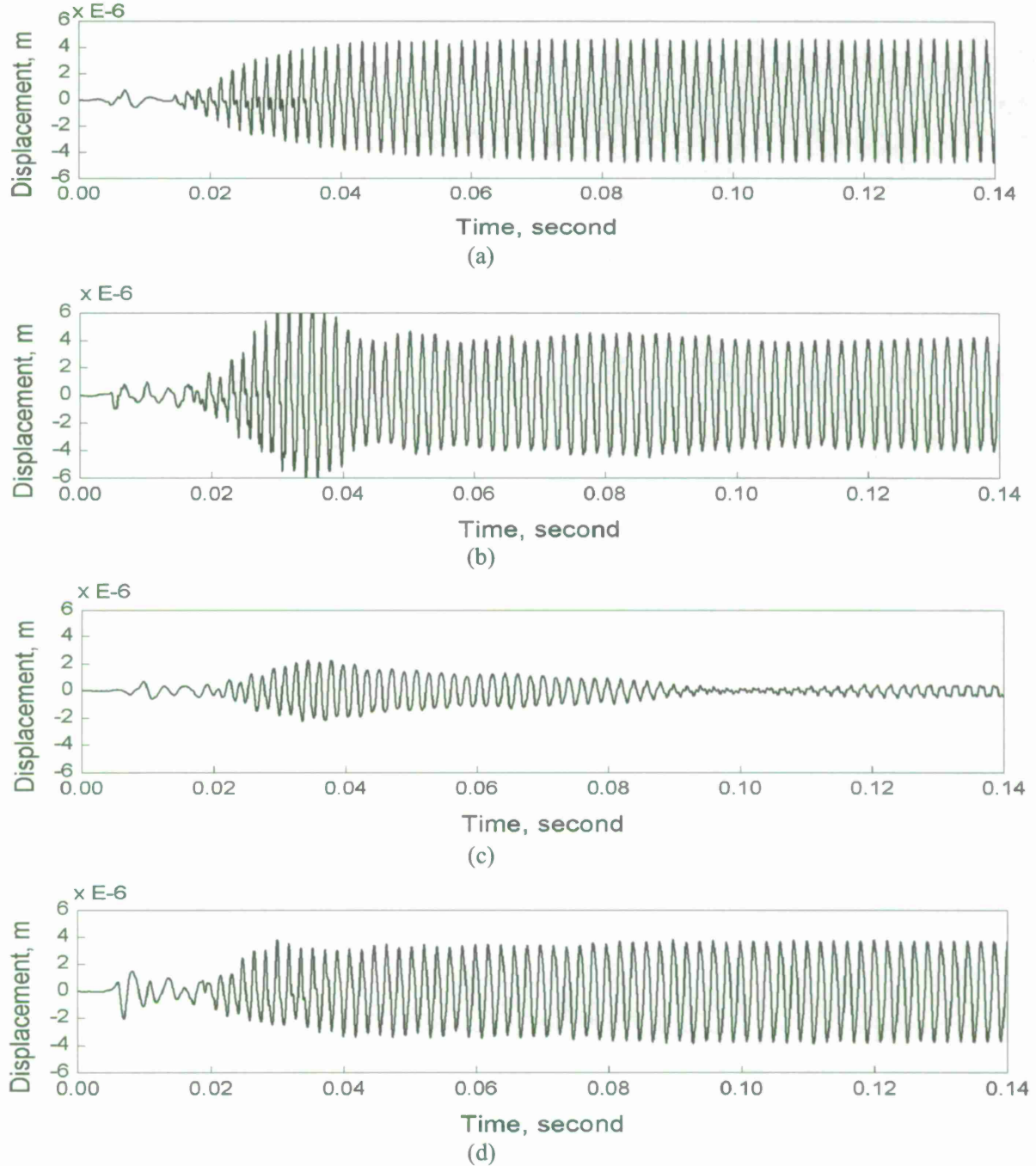


Fig. 11 Displacement time-histories obtained at a driving frequency of 497Hz. (a) input signal; (b) output signal at $x = 10\text{cm}$ for beam with resonators; (c) output signal at $x = 60\text{ cm}$ for beam with resonators; (d) output signal at $x = 60\text{ cm}$ for beam without resonators.

6. Application to Hull Slamming

To verify that our present sandwich structure with resonators can efficiently suppress vibration induced by hull slamming, one simulation is performed. Consider two long and

periodically supported sandwich beams shown in Figs. 12(a) and 12(b). One has two sections with resonators but the other does not. The interval between resonators is chosen to be 0.012m, and the number of resonators placed in the beam is 50. The cyclic impulse exhibited in Fig. 13(a) is applied to the center section of each beam, and the frequency spectrum of the impulse is depicted in Fig. 13(b). It is seen that the dominant frequency is 20 Hz. As previously mentioned, in periodically supported structures, harmonic waves can propagate only in certain frequency bands [2]. Hence, we design the supports so that the wave generated by the impulse can propagate without attenuation along the sandwich beam without resonators. Moreover, in order to show the filtering phenomenon, the local resonance frequency of resonators is selected as the dominant frequency (20 Hz) of the impulse. Figures 14(a) and 14(b) show the spectrum analysis of the responses in section (1) and section (3) of the beam without resonators, respectively. It appears that the intensity of the wave remains almost the same in both sections. Figures 15(a) and 15(b) show the responses at the same locations in the sandwich beam which contains resonators in section (2). It is observed that the intensity of the wave decreases conspicuously after it travels through section (2).

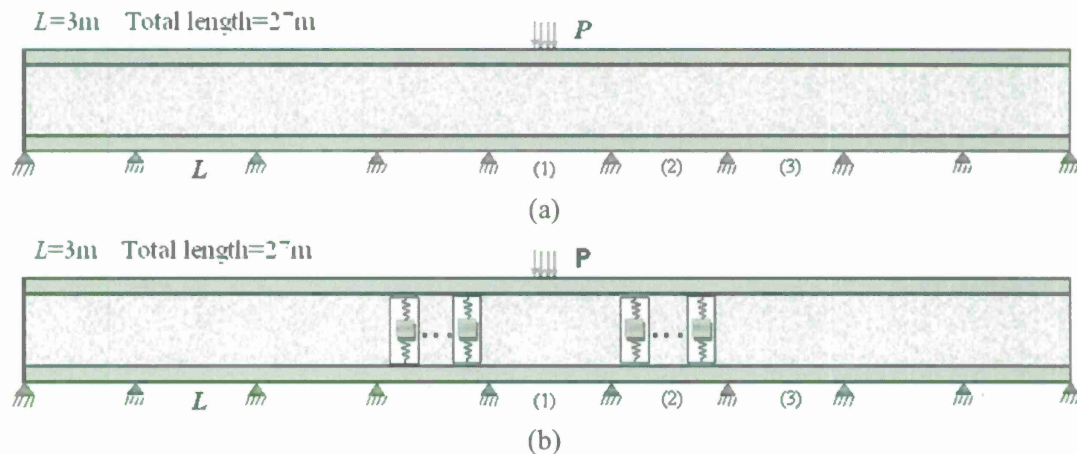


Fig. 12 (a) Supported sandwich beam with homogenous core and (b) supported sandwich beam having two sections with resonators.

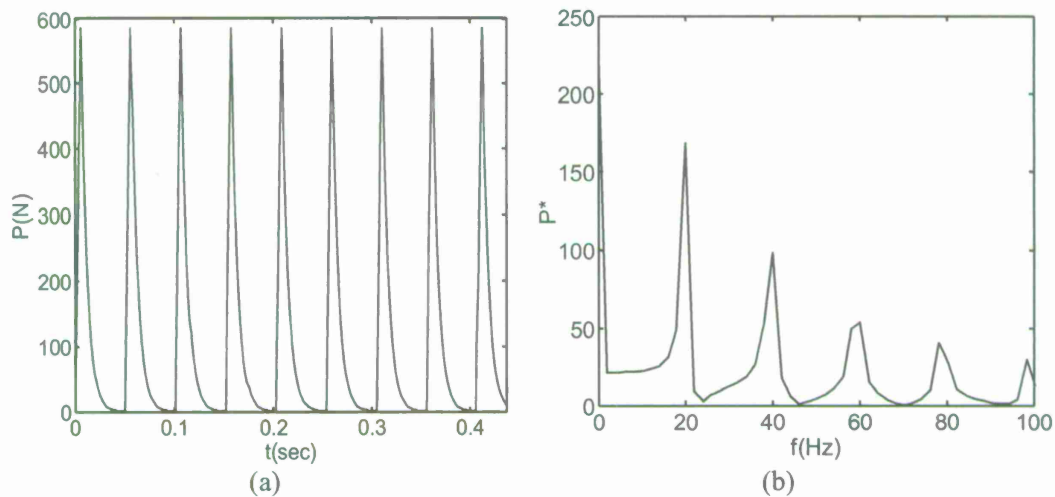


Fig. 13 (a) Cyclic loading (b) the corresponding frequency spectrum.

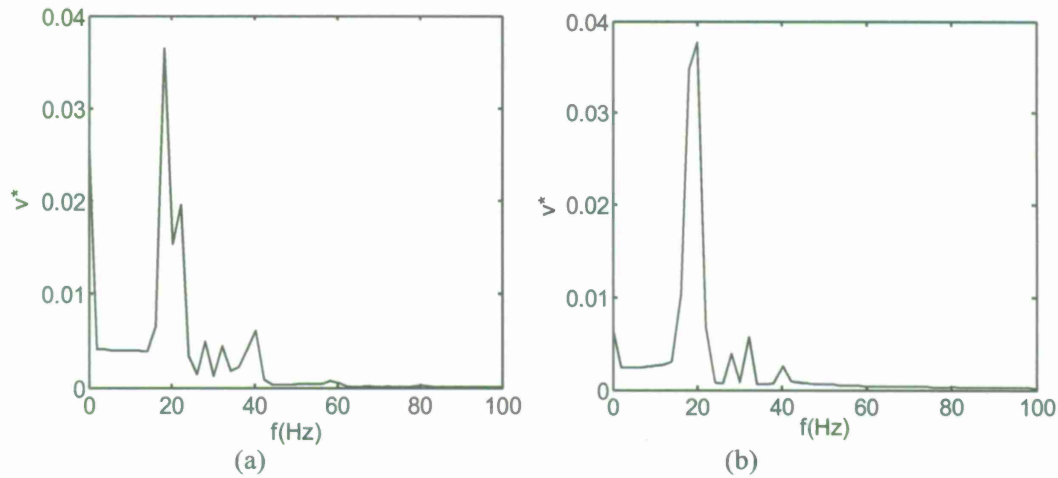


Fig. 14 Spectrum analysis of the wave (a) in section (1) and (b) in section (3) of the beam without resonators, respectively.

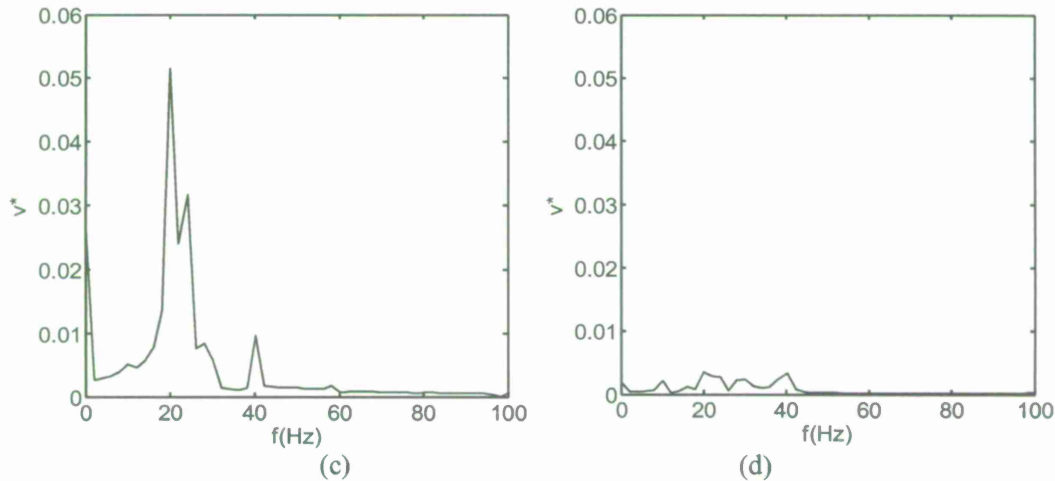


Fig. 15 Spectrum analysis of the wave (a) in section (1) and (b) in section (2) of the beam containing resonators, respectively.

7. Sandwich Beam with Periodic Cores

7.1 Introductory Remarks

Our previous work has found that sandwich structures with resonators can produce a significant effect on wave attenuation and vibration reduction. Furthermore, by choosing the local resonance frequency of the resonator, the desired location of the bandgap can be obtained. Besides the use of resonators, the work done by Mead [2-3] showed that periodic structures can produce a similar mechanism to give rise to wave attenuation. In other words, this type of periodic structure offers an alternate mechanism to stop wave propagation in sandwich structures. Following Mead's work, Ruzzene and Tsopelas [4] applied the concept of periodic structural assemblies to a sandwich plate. They found that different honeycomb core materials placed periodically in the sandwich plate are capable of obstructing the propagation of waves over specified frequency bands. The location and the extent of the stop bands can be modified by an appropriate selection of the periodicity and the geometrical and physical properties of the core. The purpose of the present study is to further investigate the dynamic characteristics of sandwich

structures consisting of periodically varying core properties and compare the efficiency of this type of sandwich beam with that of the corresponding sandwich beams with resonators. The Bloch theorem [5] is employed to find the stop bands of sandwich structures with periodic cores. Numerical examples are presented to illustrate the wave blocking behavior of the sandwich beam. The efficiencies of sandwich structures with resonators and with periodic cores, respectively, are compared.

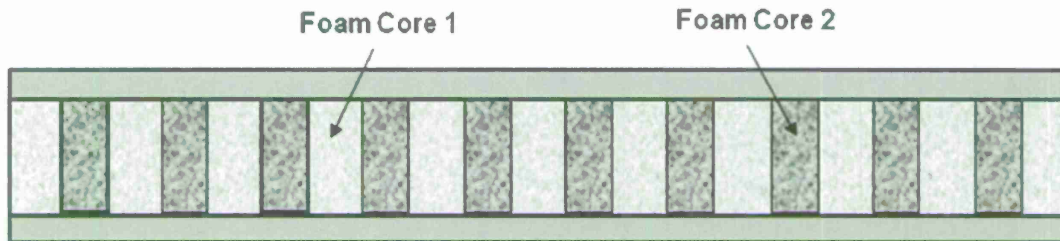


Fig. 16 An infinite sandwich beam with periodic cores

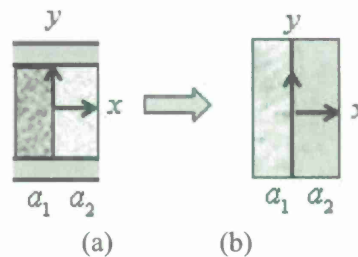


Fig. 17 The sketch of a unit cell

7.2 Dispersion Equation

Figure 16 displays the schematic of a sandwich beam with periodic core materials. A unit cell is shown in Fig. 17(a). This unit cell is regarded as a binary composite Timoshenko beam shown in Fig. 17(b). The beam is composed of an infinite repetitions of alternating section 1 with length a_1 and section 2 with length a_2 . The lattice constant is denoted by a which equals to $a_1 + a_2$. Two different core materials are used to construct the sections 1 and 2. The origin of the local coordinate is located at the junction.

The equations of motion for sections 1 and 2 are given by

$$(GA)^{(r)}[v^{(r)}(x, t) + \varphi^{(r)}(x, t)] - (\rho A)^{(r)} \ddot{v}^{(r)}(x, t) = 0 \quad (9)$$

$$(EI)^{(r)} \varphi^{(r)}(x, t) - (GA)^{(r)}[v^{(r)}(x, t) + \varphi^{(r)}(x, t)] - (\rho I)^{(r)} \ddot{\varphi}^{(r)}(x, t) = 0 \quad (10)$$

where $r = 1, 2$ for distinguishing section 1 from section 2, $(EI)^{(r)}$ denotes bending rigidity, $(GA)^{(r)}$ is shear rigidity, $(\rho A)^{(r)}$ is mass per unit length, $v(x, t)$ is vertical displacement, and $\varphi(x, t)$ is rotation of the cross-section of the sandwich beam. By assuming a general harmonic wave propagating in the sandwich beam, two displacement functions v and φ can be expressed in the wave form $e^{i(qx - \omega t)}$ in which q is wave number and ω is angular frequency. Using the technique of separation of variables, displacement $v(x, t)$ and rotation $\varphi(x, t)$ can be expressed as $\hat{v}(x)e^{-i\omega t}$ and $\hat{\varphi}(x)e^{-i\omega t}$, respectively. Substituting these two functions in Eqs. (9) and (10) yields the general solutions of the form:

$$\hat{v}^{(r)}(x) = D_1^{(r)} e^{ik_1^{(r)}x} + D_2^{(r)} e^{ik_2^{(r)}x} + D_3^{(r)} e^{ik_3^{(r)}x} + D_4^{(r)} e^{ik_4^{(r)}x} \quad (11)$$

$$\hat{\phi}^{(r)}(x) = R_1^{(r)} e^{ik_1^{(r)}x} + R_2^{(r)} e^{ik_2^{(r)}x} + R_3^{(r)} e^{ik_3^{(r)}x} + R_4^{(r)} e^{ik_4^{(r)}x} \quad (12)$$

where $D_l^{(r)}$ are constant amplitudes and

$$R_l^{(r)} = D_l^{(r)} \{ (GA)^{(r)} [k_l^{(r)}]^2 - (\rho A)^{(r)} \omega^2 \} / [i (GA)^{(r)} k_l^{(r)}] \text{ for } l = 1, 2, 3, 4.$$

At the junction ($x = 0$) between the two core elements, continuities of deflection, rotation, moment and shear force must be satisfied as follows:

$$\hat{v}^{(2)}(0) = \hat{v}^{(1)}(0) \quad (13)$$

$$\hat{\phi}^{(2)}(0) = \hat{\phi}^{(1)}(0) \quad (14)$$

$$\hat{\psi}^{(2)}(0) = \hat{\psi}^{(1)}(0) \quad (15)$$

$$(GA)^{(2)} [\hat{v}^{(2)}(0) + \hat{\phi}^{(2)}(0)] = (GA)^{(1)} [\hat{v}^{(1)}(0) + \hat{\phi}^{(1)}(0)] \quad (16)$$

Due to the periodicity of the infinite structure in the x direction, the displacement, rotation, moment, and shear force also have to obey the Bloch theorem [5], namely,

$$\hat{v}^{(2)}(a_2) = e^{iqa} \hat{v}^{(1)}(-a_1) \quad (17)$$

$$\hat{\phi}^{(2)}(a_2) = e^{iqa} \hat{\phi}^{(1)}(-a_1) \quad (18)$$

$$\hat{\psi}^{(2)}(a_2) = e^{iqa} \hat{\psi}^{(1)}(-a_1) \quad (19)$$

$$(GA)^{(2)} [\hat{v}^{(2)}(a_2) + \hat{\phi}^{(2)}(a_2)] = e^{iqa} (GA)^{(1)} [\hat{v}^{(1)}(-a_1) + \hat{\phi}^{(1)}(-a_1)] \quad (20)$$

where q is wave number. Eqs. (13) - (20) form a standard eigenvalue problem from which the dispersion relationship between wave frequency ω and wave number q is obtained. For a given ω , the values of q are obtained from solving this dispersion equation. Depending on whether q is real or complex, pass bands or stop bands are determined.

7.3 Dispersion Curves and Stop Bands

Table 1 lists the dimensions and material constants adopted in the computation, and the corresponding sandwich beam properties are listed in Table 2. The face sheet is AS43501-6 carbon/epoxy composite laminate $[0_2/90_2/0_2]$ with an effective elastic Young's modulus E_F ; and the core material is Rohacell IG-51 foam. The thickness of the face sheet and that of the core are denoted by h_F and h_c , respectively, and the width of the beam is denoted by b . The densities of the face sheet and the core are 1550 kg/m^3 and 52.1 kg/m^3 , respectively.

Table 1 Dimensions and material constants of specimen.

| $E_f(\text{GPa})$ | $h_f(\text{m})$ | $h_c(\text{m})$ | $b(\text{m})$ |
|-------------------|-----------------------|-----------------------|---------------|
| 97.19 | 7.62×10^{-4} | 3.02×10^{-2} | 0.019 |

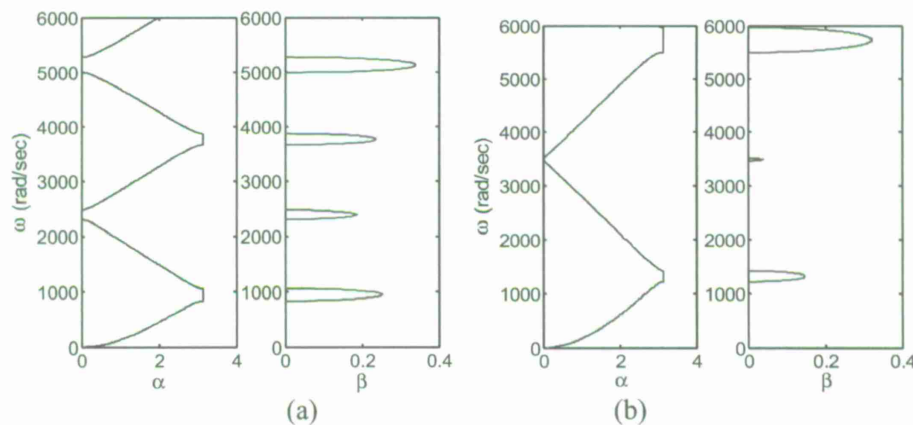
Table 2 Effective properties of the sandwich beam.

| $EI(\text{Pa} \cdot \text{m}^4)$ | $GA(\text{Pa} \cdot \text{m}^2)$ | $\rho A(\text{kg/m})$ | $\rho I(\text{kg} \cdot \text{m})$ |
|----------------------------------|----------------------------------|-----------------------|------------------------------------|
| 677 | 1.15×10^4 | 0.075 | 1.31×10^{-5} |

Consider an infinite sandwich beam with periodic foam cores. The lattice constant is chosen to be $a = 0.75\text{m}$, and $a_1 = a_2 = 0.375\text{m}$. Four sandwich beams are considered in order to show the effect of shear rigidity and mass density on the dispersion curves. Table 3 lists the properties of these four beams. Figures 18(a), 18(b), 18(c), and 18(d) show the dispersion curves for the four sandwich beams, respectively. α and β denote, respectively, the real part and imaginary part of the dimensionless wave number, namely $\bar{q} = qa = \alpha + i\beta$. It is concluded that Beam III is more capable of enlarging the stop band and increasing the value of β than the other three beams. In Fig. 18(d), it is noted that the width of frequency in the stop bands becomes very narrow. That is, increasing the ratio of the shear rigidities of the two cores while decreasing that of the mass densities with the same proportion yields little effect on wave attenuation. Another important finding is that a larger lattice constant leads to lower frequencies in the stop band.

Table 3 Ratios of shear rigidities and mass densities for four sandwich beams

| | Beam I | Beam II | Beam III | Beam IV |
|-----------------|--------|---------|----------|---------|
| ρ_2/ρ_1 | 4 | 1 | 4 | 1/4 |
| $(GA)_2/(GA)_1$ | 1 | 4 | 4 | 4 |



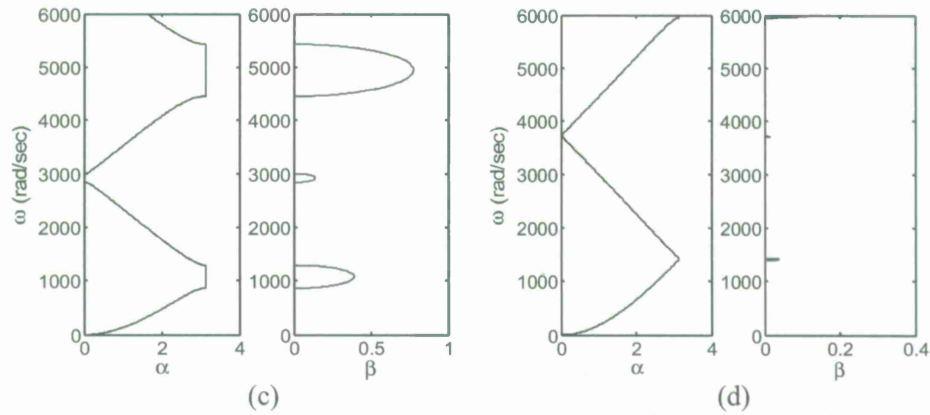
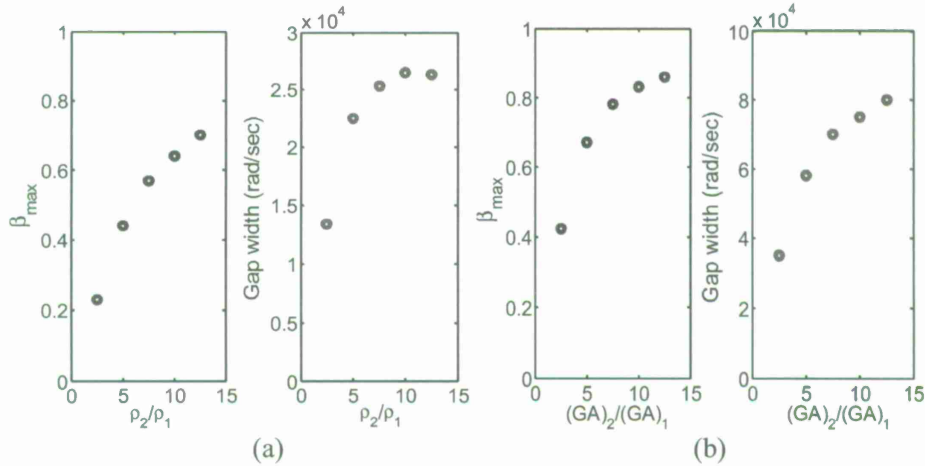


Fig. 18 Dispersion curves of (a) Beam I, (b) structure Beam II, (c) beam III, and (d) Beam IV.

The results in Fig. 18 indicate that mass density or shear rigidity of the sandwich core can change the magnitude of β as well as modify the location and width of the stop bands. Hence, we further conduct an investigation in the effect of ρ_2/ρ_1 and that of $(GA)_2/(GA)_1$ on the maximum value of β and the gap width of stop bands in sandwich beams with periodic cores. We take the lattice constant to be 0.012m, i.e., $a_1 = a_2 = 0.006m$. Figure 19 shows the variation of β_{max} and the bandgap width for the first stop band with varying properties of the core. In Fig. 19(a), the shear rigidities of the two cores are chosen to be identical, the ratio of mass density is assumed to be 2.5, 5, 7.5, 10, or 12.5. Conversely, in Fig. 19(b), the densities of the two core materials are assumed identical, and the ratio $(GA)_2/(GA)_1$ varies from 2.5 to 12.5. In Fig. 19(c), ρ_2/ρ_1 and $(GA)_2/(GA)_1$ are assumed to be equal and both vary from 2.5 to 12.5. It is found that the larger ratio ρ_2/ρ_1 or $(GA)_2/(GA)_1$ is taken, the larger β_{max} is obtained. It is also observed that among the three cases, the last one can give the largest β_{max} and the widest frequency gap.



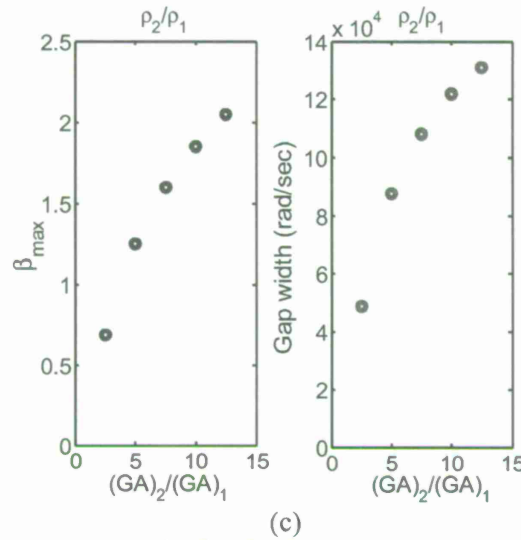


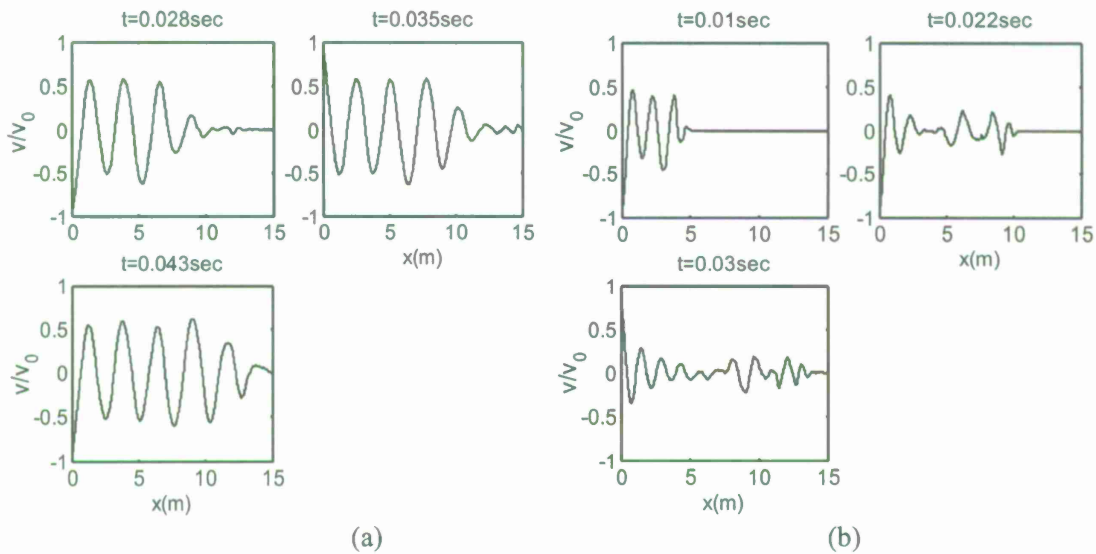
Fig. 19 Effect of the ratio ρ_2/ρ_1 or $(GA)_2/(GA)_1$ on β_{max} and the width of the 1st band gap.

7.4 Simulation of Wave Attenuation

To capture the attenuation behaviour of wave propagation, consider a 15m long sandwich beam actuated at the left end with the prescribed displacement history given by

$$v(t) = v_0 \sin \omega t \quad t \geq 0 \quad (13)$$

The material properties of Beam III are used to perform the computation. Figures 20(a), 20(b), and 20(c) show the wave motions in the sandwich beam excited with three different driving frequencies, 400 rad/sec, 1080 rad/sec, and 4945 rad/sec, respectively. The first excitation frequency is located within the 1st pass band; the second one is within the 1st stop band; the third is within the 3rd stop band. As expected, wave amplitude is significantly reduced with distance in the last two cases. In contrast, there is no considerable wave attenuation found in the first case. It is also found that a larger value of β gives a greater reduction in wave amplitude.



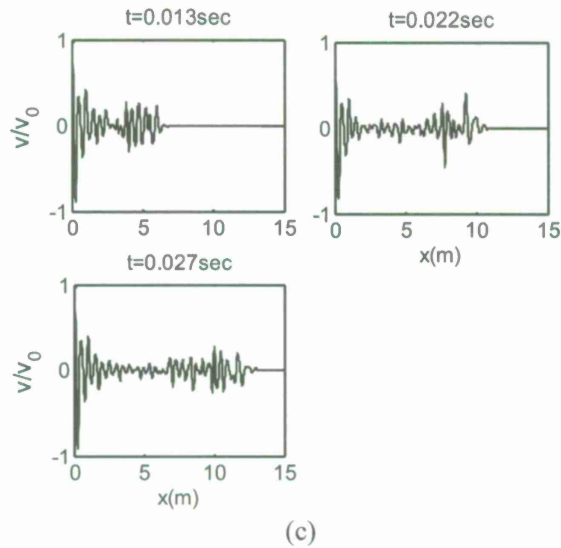


Fig. 20 Mode shape at different times for (a) $\omega = 400$ rad/sec, (b) $\omega = 1080$ rad/sec, (c) $\omega = 4945$ rad/sec.

7.5 Wave Filtering

The sandwich structure with a periodic core can be used as a band filter. For illustration, a sandwich beam having a section with periodic cores as shown in Fig. 21 is studied. Sixteen unit cells of periodic core are embedded in the sandwich beam. An excitation of the form given by Eq. (13) with a dominant frequency is applied at the left end of the beam. The actuation frequency is 1080 rad/sec, same as the one considered in Fig. 20(b).

Figure 22 shows the comparison of the responses of the beams with and without periodic cores, respectively. It is found that, initially, the responses are identical. However, after the wave passes through the section with periodic cores, the wave amplitude is significantly reduced. In contrast, no appreciable change in wave amplitude is seen in the sandwich without periodic cores. It is also noted that there is a significant reflection of incident wave from the section with periodic cores to the section without periodic cores.

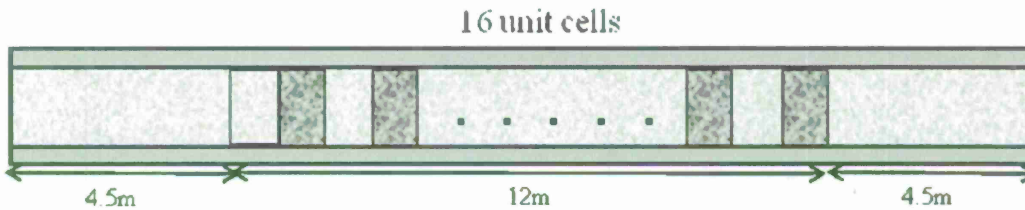


Fig. 21 Sandwich beam with a section containing periodic cores

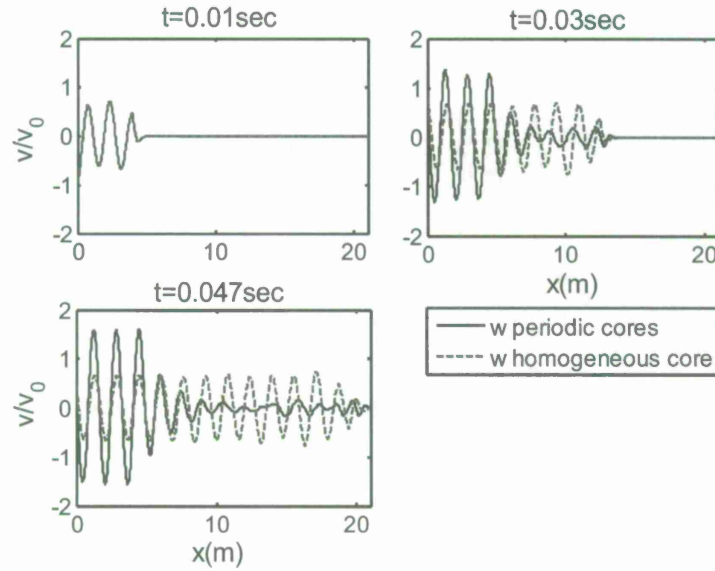


Fig. 22 Wave profiles of sandwich beam with and without periodic cores

8. Comparison of Sandwich Structures with Resonators and with Periodic Cores

Both sandwich structures with resonators and with periodic cores are capable of stopping waves with certain frequencies from propagating into the beam. It is of interest to compare the efficiencies in wave attenuation between these two types of sandwich constructions.

In order to objectively compare the efficiency in wave attenuation and the width of the generated bandgap between a sandwich beam with periodic cores and that with resonators, the mass densities of the two beams must be set equal. Consider the unit cells of the two types of sandwich beams as shown in Fig. 23. The unit length a is chosen as 0.048m. The total mass varies with different ratios ρ_2/ρ_1 as discussed in Fig 19(a), but here the density ratios are taken as 5.0, 10.0, 15.0, and 20.0 instead.

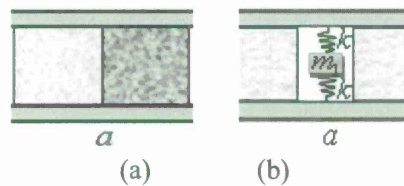


Fig. 23 Sandwich structure (a) with periodic cores (b) with resonators.

The local resonance frequency of resonators ω_0 for the beam with resonators is selected to be the same as the optimized frequency ω_c which produces the maximum attenuation factor β in the beam with periodic cores, i.e., $\omega_0 = \omega_c$. Using the 1st band gap as an example, Fig. 24(a) displays the variation of β_r/β_c ratio with varying wave frequency and mass density. β_r and β_c denote the attenuation factors of the two sandwich beams, respectively, and $\bar{\omega} = \omega/\omega_0 = \omega/\omega_c$. It is seen that as $\bar{\omega} \rightarrow 1$, β_r/β_c becomes very large, and that even at a distance away from $\bar{\omega} = 1$, the difference between the two decay factors remains quite substantial. In other words, resonators always provide much better efficiency in wave attenuation than periodic cores. In Fig. 24(b), it is obvious that, for the beam with resonators, the bandgap width is proportional to the ratio of core mass densities. In contrast, for the beam with periodic cores, the gap width grows more slowly. It

is concluded that increasing the ratio of densities of cores might not lead to a wider gap. One can also conclude that with the same weight of the beam, resonators may make a greater impact on wave attenuation. Figure 19 gives such example. The actuation (see Eq. (13)) is given in terms of a prescribed displacement applied to the respective left ends of the two beams. The applied frequency is $\omega = 1.1\omega_0$. The ratio of mass densities is chosen to be 8.6, namely, the last case in Fig. 18(a). Figures 25(a) and 25(b) show, respectively, the deformed shapes of the first 1 m of the sandwich beams at elapsed time of 0.0097sec, after actuation begins. It is evident that for the beam with resonators, a sharp spatial decay of amplitude of the flexural motion takes place whereas for the beam with periodic cores, decay is much more gradual.

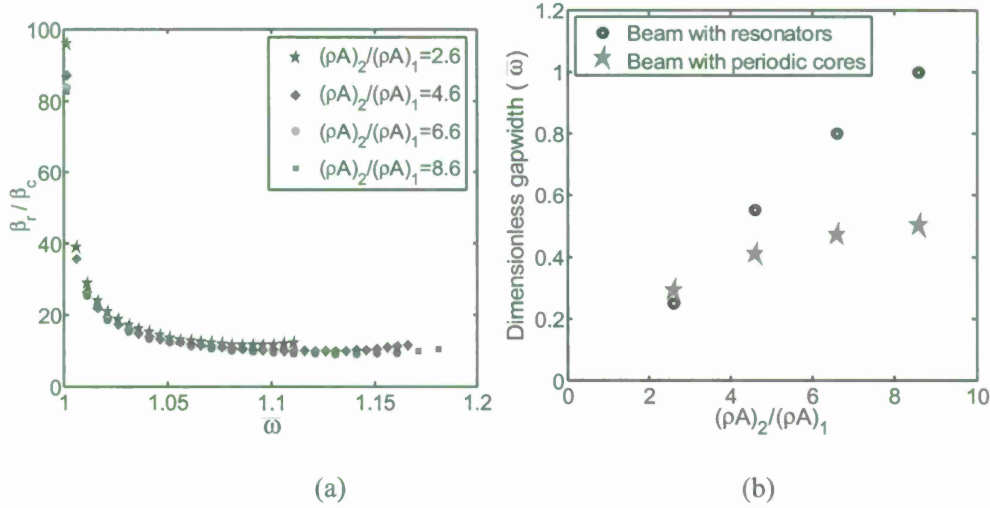
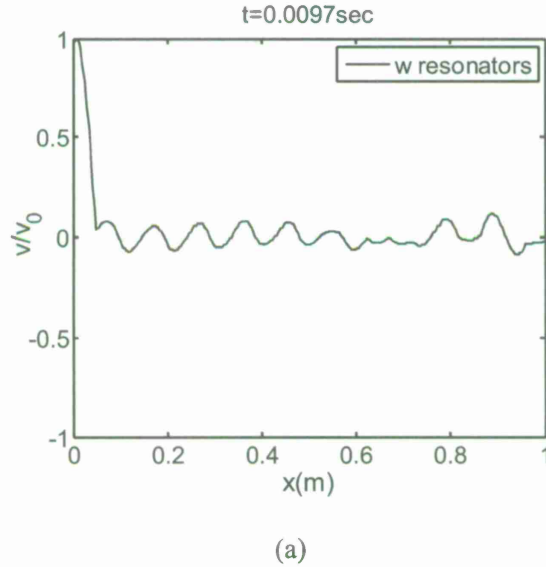


Fig. 24 Comparison between two types of sandwich beams for (a) β ratio, and (b) the gapwidth.



(a)

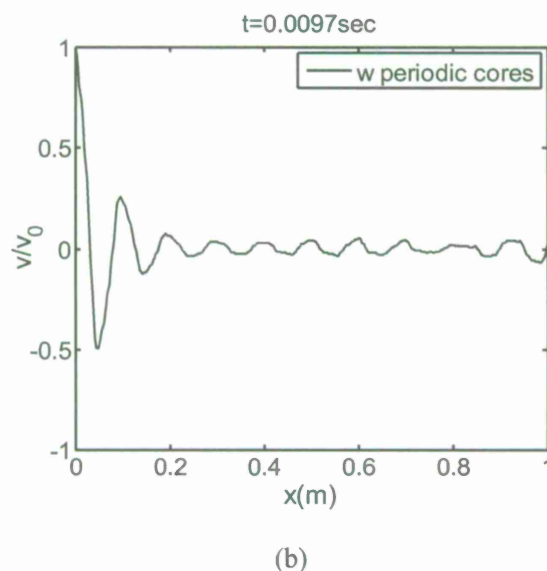


Fig. 25 Wave profile at elapsed time of 0.0097sec for (a) beam with resonators, and (b) beam with periodic cores.

9. Conclusion

The dynamic behavior of sandwich beams containing resonators was investigated analytically and experimentally. It was found that, near the local resonance frequency of the resonator, harmonic waves cannot propagate without attenuation in amplitude and that the extent of the bandgap can be selected by altering the local resonance frequency of the resonator. Also, the magnitude of the internal mass has a greater influence on the size of the bandgap than the spring constant of the resonator. It is concluded that the sandwich structure with resonators is capable of efficiently blocking waves in a certain frequency range near the local resonance frequency of the resonator.

In this study, it was shown that sandwich beams with resonators embedded in the core or with periodic core properties can produce stop bands to forbid wave propagation. For the sandwich beam with a periodic core to obtain large bandgap widths, the ratio of densities and that of rigidities of the two core materials must have the same proportion. Based on the comparison between beams with periodic cores and beams with resonators, it is concluded that the latter is more efficient in effecting wave attenuation and vibration reduction. Moreover, the desired bandgap can be easily achieved by selecting the local resonance frequency of resonators. This is especially true for low frequency bandgaps.

10. References

- [1] J.S. Jensen, Phononic band gaps and vibrations in one- and two-dimensional mass-spring structures, *Journal of Sound and Vibration* 266 (2003) 1053-1078.
- [2] D.J. Mead, Free wave propagation in periodically supported infinite beams, *Journal of Sound and Vibration* 11 (1970) 181-197.
- [3] D.J. Mead, A new method of analyzing wave propagation in periodic structures:

applications to periodic Timoshenko beams and stiffened plates, *Journal of Sound and Vibration* 104 (1986) 9-27.

[4] Massimo Ruzzene and Panos Tsopelas, Control of wave propagation in sandwich plate row with periodic honeycomb core, *Journal of Engineering Mechanics* 129 (2003) 975-986.

[5] C. Kittel, *Introduction to Solid State Physics*, Wiley, New York, 1986.